J. Fluid Mech. (1999), *vol.* 381, *pp.* 305–335. Printed in the United Kingdom

Mechanics of nonlinear short-wave generation by a moored near-surface buoy

By Q. ZHU, Y. LIU, A. A. TJAVARAS†, M. S. TRIANTAFYLLOU AND D. K. P. YUE‡

Department of Ocean Engineering, Massachusetts Institute of Technology, Cambridge, MA 02139, USA

(Received 14 May 1998 and in revised form 5 October 1998)

We consider the nonlinear interaction problem of surface waves with a tethered near-surface buoy. Our objective is to investigate mechanisms for nonlinear short surface wave generation in this complete coupled wave–buoy–cable dynamical system. We develop an effective numerical simulation capability coupling an efficient and high-resolution high-order spectral method for the nonlinear wave–buoy interaction problem with a robust implicit finite-difference method for the cable–buoy dynamics. The numerical scheme accounts for nonlinear wave–wave and wave–body interactions up to an arbitrary high order in the wave steepness and is able to treat extreme motions of the cable including conditions of negative cable tension. Systematic simulations show that beyond a small threshold value of the incident wave amplitude, the buoy performs chaotic motions, characterized by the snapping of the cable. The root cause of the chaotic response is the interplay between the snapping of the cable and the generation of surface waves, which provides a source of strong (radiation) damping. As a result of this interaction, the chaotic buoy motion switches between two competing modes of snapping response: one with larger average peak amplitude and lower characteristic frequency, and the other with smaller amplitude and higher frequency. The generated high-harmonic/short surface waves are greatly amplified once the chaotic motion sets in. Analyses of the radiated wave spectra show significant energy at higher frequencies which is orders of magnitude larger than can be expected from nonlinear generation under regular motion.

1. Introduction

Extensible cables have been widely used to position or tow floating facilities such as offshore platforms, ships and buoys in the ocean. Most previous studies on the subject of the dynamics of tethered objects in waves have been limited to the prediction of hydrodynamic loads on the structures and mooring systems. In the present study, our main interest is the mechanisms of generating short free-surface waves by the motion of moored near-surface objects which may be detectable by remote sensing. For specificity, we consider the dynamics of a single near-surface spherical buoy tethered to the bottom by a synthetic cable. We consider the nonlinear response of the cable–buoy system subject to the influence of a regular incident wave and the nonlinear free-surface pattern that results.

† Currently with Exxon Production Research Co., Houston, Texas, USA.
‡ Author to whom correspondence should be addressed.

The problem we pose requires the effective solution of two coupled dynamical problems. First is the nonlinear dynamics of a body interacting with ambient surface waves. This problem for floating or submerged bodies is classical and has been studied extensively. For large-amplitude (and arbitrary) body motions, the general nonlinear problem must be solved numerically in the time domain, and three-dimensional results are still quite limited (see e.g. Tsai & Yue 1996 for a review). The other problem is that of a cable in arbitrary motion wherein both transverse and longitudinal motions are important as well as the effect of bending stiffness when tension in the cable becomes zero or negative. Despite the complexity, such simulations have recently become possible (see e.g. Triantafyllou 1994 for a review).

The present work combines these two capabilities in nonlinear wave–body interactions and tether mechanics to study the coupled dynamics of a submerged buoy. Of special interest are the nonlinear mechanisms for the generation of surface disturbances particularly in the higher-harmonic short-wavelength (relative to incident waves) regime. Through our investigation, we identify two classes of mechanisms for nonlinear short-wave generation.

(1) For relatively small buoy–tether motions, wherein the (positive) tension in the cable is maintained, higher-harmonic surface waves are generated mainly via nonlinear (sum-frequency) wave–wave and wave–body interaction mechanisms. The amplitude of the mth harmonic wave is, in general, $O(\epsilon^m)$, where ϵ measures the incident wave steepness. Although, the mth harmonic wave can be as short as m^{-2} that of the incident wave and may occur where there is an absence of ambient wave energy, the amplitudes are increasingly small for larger m. Thus, this represents a relative weak mechanism for detectable short waves.

(2) When the incident wave amplitude increases above a certain threshold, we find a new cable–buoy–wave interaction mechanism wherein the cable tension may alternately vanish and increase rapidly to large values in a cable 'snapping' motion. The resulting buoy motion is in general chaotic and imparts a substantial amount of energy into surface waves in a broad frequency range. Our calculations show, for instance, appreciable radiated energy in frequencies as high as $m \sim O(10)$ for $\epsilon \sim O(0.1)$ and realistic cable–buoy properties/configuration. This is therefore a novel and highly efficient mechanism for short-wave generation by a submerged tethered body.

In § 2, we describe the physical problem and the mathematical formulations for the wave–body interaction problem and the cable dynamic problem. To solve this coupled hydrodynamic and dynamic interaction problem, we develop an effective numerical scheme in § 3 by coupling an efficient high-order spectral method for the nonlinear wave–body interaction (Liu 1994) and an implicit finite-difference method for the nonlinear cable response (Tjavaras *et al.* 1998). In § 4, we present the simulation results showing the regular and chaotic responses of the tethered buoy. Of special interest are the free-surface wave patterns created by these motions, which are analysed. We conclude in § 5.

2. Formulation of the nonlinear wave–buoy–cable interaction problem

The physical system under study consists of a near-surface buoy tethered to the bottom through an extensible cable (see figure 1). Under the influence of incident surface waves, the cable–buoy system is subject to oscillatory forces and is excited; its motions, in turn, create free-surface waves. Our interests are the dynamics of the tethered-buoy motion and the characteristics of the resulting radiated waves.

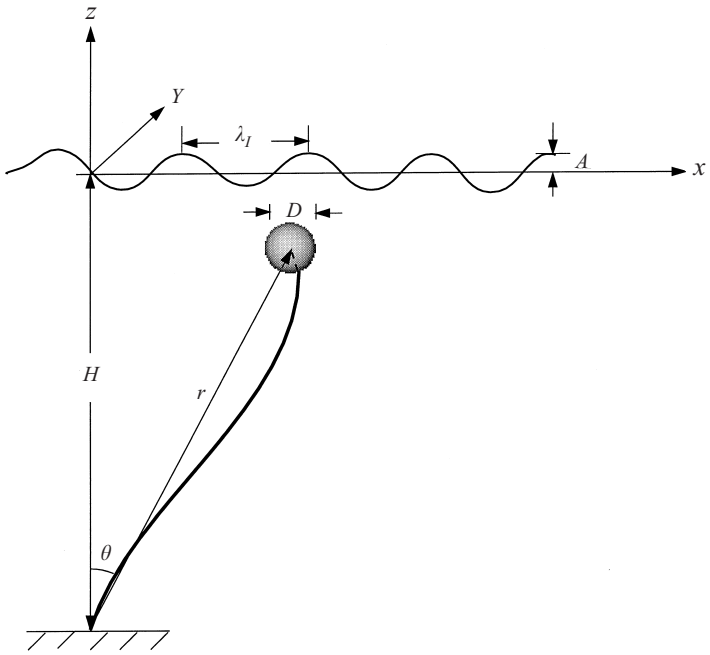

FIGURE 1. A near-surface tethered buoy under waves.

For the present study, the nonlinear wave–body interaction problem is solved in the context of potential flow and arbitrary body motions in the time domain. Viscous effects on the body and the cable are accounted for with simple models of (constant) drag coefficients in Morison's formula applied using relative velocity including wave and body motions. Within this context, the problem is treated in its generality, including all nonlinearities for a three-dimensional response and wave generation.

For specificity, we consider a spherical buoy, diameter D. We assume a constant density for the sphere, ρ_s, which is less than the water density ρ. The sphere is attached at the centre to the upper end of a cable so that, in the absence of waves, the centre of the sphere is at a distance h below the mean free surface. The lower end of the cable is fixed on the bottom at a depth H.

We define a Cartesian coordinate system with z-axis vertical and positive upwards, $z = 0$ coinciding with the undisturbed free surface. We assume that the cable–buoy system is subject to the action of harmonic uni-directional incident waves, wavelength λ_I, in the (x, z)-plane. Even under planar wave excitation, the motion of the cable–buoy system may not be planar due to three-dimensional instability (cf. Tjavaras *et al.* 1998). In this case, the position of the centre of the sphere is denoted by its Cartesian coordinates (X, Y, Z). If the motion is (assumed) planar, it is convenient to define the polar coordinates of the body centre, (r, θ), defined in the (x, z)-plane with respect to the bottom attachment point $(0, 0, -H)$ (see figure 1). In this paper, we focus primarily on the planar motion case. The possibility of out-of-plane motions is discussed in § 5.

The problem of nonlinear wave interactions with a tethered near-surface buoy consists of two separate hydrodynamic problems which are coupled through the motion of the buoy. The first problem involves wave diffraction and radiation by the buoy; the second problem involves the mechanics of the cable under surface waves.

These two problems are coupled at the buoy–tether interconnection, hence ultimately their simulation requires coordinated simulation of both problems.

2.1. *Equation of motion for the buoy*

The motion of the buoy is governed by Newton's second law:

$$\mathscr{M}\frac{\mathrm{d}^2\boldsymbol{X}}{\mathrm{d}t^2} = \boldsymbol{B} - \boldsymbol{W} + \boldsymbol{F}_B + \boldsymbol{T}, \tag{2.1}$$

where $\boldsymbol{X} \equiv (X, Y, Z)$ denotes the centre position of the buoy, t the time, $\mathscr{M}$ the mass of the buoy, $\boldsymbol{B}$ the buoyancy force on the buoy, $\boldsymbol{W}$ the weight of the buoy, $\boldsymbol{F}_B$ the hydrodynamic force on the buoy, and $\boldsymbol{T}$ the tension of the cable at the connection with the buoy centre.

Equation (2.1) for the buoy motion couples the wave–buoy interaction problem and the cable–buoy dynamic problem. The position and velocity of the buoy, $\boldsymbol{X}$ and $\dot{\boldsymbol{X}} \equiv \boldsymbol{V}_B$, determine the diffracted and radiated wavefields and the hydrodynamic force $\boldsymbol{F}_B$. At the same time, the magnitude and direction of the cable tension force $\boldsymbol{T}$ is given by the solution of the cable dynamics for specified $\boldsymbol{X}$ and $\dot{\boldsymbol{X}}$ (and cable position and velocity).

2.2. *Hydrodynamic force on the buoy*

The hydrodynamic force on the body $\boldsymbol{F}_B$ consists in general of a potential flow contribution associated with wave diffraction and radiation, $\boldsymbol{F}_B^{\Phi}$; and a viscous drag effect associated with vortex shedding, $\boldsymbol{F}_B^{v}$. The latter is generally unimportant in the absence of current, and for small to moderate Keulegan–Carpenter number $K_c \equiv 2\pi \mathrm{e}^{-k_I h} A/D$, where k_I, A are the incident wavenumber and wave amplitude.

For the potential flow contribution, we formulate the wave–buoy interaction problem in terms of the velocity potential $\Phi(\boldsymbol{x}, t)$ which satisfies Laplace's equation ($\nabla^2\Phi = 0$) inside the fluid. On the instantaneous free surface, denoted by $z = \zeta(x, y, t)$, Φ satisfies the nonlinear kinematic and dynamic boundary conditions:

$$\left.\begin{aligned} &\zeta_t + \Phi_x\zeta_x + \Phi_y\zeta_y - \Phi_z = 0, \\ &\Phi_t + \tfrac{1}{2}|\nabla\Phi|^2 + g\zeta = 0, \end{aligned}\right\} \tag{2.2}$$

where g is the gravitational acceleration. On the body, $S_B(t)$, the no-flux condition applies

$$\frac{\partial\Phi}{\partial n} = \boldsymbol{n}\cdot\boldsymbol{V}_B \quad \text{on} \quad S_B(t) \tag{2.3}$$

where $\boldsymbol{n} = (n_x, n_y, n_z)$ is the unit normal into the body. On the bottom, $z = -H$, we have $\Phi_z = 0$, or $\nabla\Phi \to 0$ as $z \to -\infty$ for deep water ($H \gg \lambda_I$).

For initial conditions, at $t = 0$, the free-surface elevation and velocity potential as well as the position and velocity of the body are prescribed, typically quiescent conditions for the flow and equilibrium position for the cable–buoy system. The initial-boundary-value problem for the velocity potential Φ is complete with the imposition of a radiation condition at the far field, in this case, a physical argument that the diffracted and radiated waves by the body propagate away from the body.

In terms of the velocity potential Φ, the hydrodynamic pressure (P) on the buoy is determined according to Bernoulli's equation:

$$\frac{P}{\rho} = -\Phi_t - \tfrac{1}{2}\nabla\Phi\cdot\nabla\Phi. \tag{2.4}$$

The wave force $\boldsymbol{F}_B^{\Phi}$ on the buoy is obtained by integration of the pressure over the body surface:

$$\boldsymbol{F}_B^{\Phi} = \rho \int\int_{S_B} (\Phi_t + \tfrac{1}{2}\nabla\Phi \cdot \nabla\Phi)\boldsymbol{n}\, \mathrm{d}s. \tag{2.5}$$

To account for the flow separation effect, we include a viscous drag force on the body which we estimate using a quadratic (Morison's) formula:

$$\boldsymbol{F}_B^{v} = -\tfrac{1}{2}\rho C_D A_p (\boldsymbol{V}_B - \nabla\Phi_I)|\boldsymbol{V}_B - \nabla\Phi_I| \tag{2.6}$$

where C_D is the drag coefficient and A_p the projected area of the body, Φ_I is the velocity potential for the incident wave field, and $\nabla\Phi_I$ is evaluated at the centre of the body. Note that the treatment (2.6) for the viscous force on the body is consistent with that for the cable (§ 2.3). For the problem we consider, the force on the body is dominated by $\boldsymbol{F}_B^{\Phi}$ and the inclusion of (2.6) has in fact minimal effect on the final results.

For $K_c \gg 1$, the hydrodynamic load is dominated by flow separation and added-mass effects and the wave diffraction and radiation effect is negligible. In this case, a simple model can be written for the total hydrodynamic force $\boldsymbol{F}_B$ with (2.5) replaced by an added-mass term only, namely Morison's formula:

$$\boldsymbol{F}_B = -\mathscr{M}_a \frac{\mathrm{d}}{\mathrm{d}t}(\boldsymbol{V}_B - \nabla\Phi_I) + \rho\mathscr{V}\frac{\mathrm{d}}{\mathrm{d}t}\nabla\Phi_I - \tfrac{1}{2}\rho C_D A_p (\boldsymbol{V}_B - \nabla\Phi_I)|\boldsymbol{V}_B - \nabla\Phi_I| \tag{2.7}$$

where the substantial derivative $\mathrm{d}/\mathrm{d}t \equiv \partial/\partial t + (\nabla\Phi_I - \boldsymbol{V}_B)\cdot\nabla$, $\mathscr{M}_a$ is the added mass of the buoy, and $\mathscr{V}$ the volume of the buoy. On the right-hand side of (2.7), the first term represents the added-mass force, the second term the buoyancy force due to the unsteady ambient flow, and the third term the viscous drag force.

2.3. *Equations for the cable dynamics*

We model the cable as a slender rod and describe the cable motion in terms of its centreline. The equations of motion for the cable include the balance of forces, the balance of moments and the compatibility of the cable geometry. To avoid the ill-posed problem when the tension of the cable becomes vanishingly small or negative (Triantafyllou & Howell 1994), the bending stiffness of the cable is included.

We define a local Lagrangian reference frame with three unit vectors $\hat{\boldsymbol{\tau}}$, $\hat{\boldsymbol{n}}$, and $\hat{\boldsymbol{b}}$ in the tangential, normal, and bi-normal directions of the cable, respectively. Each point along the cable is represented by its Lagrangian coordinate s which is equal to the physical length of the cable from the low (attachment) point. This Lagrangian reference frame can be related to the space-fixed Cartesian coordinate system (x, y, z) by the relation:

$$\begin{bmatrix} \hat{\boldsymbol{\tau}} \\ \hat{\boldsymbol{n}} \\ \hat{\boldsymbol{b}} \end{bmatrix} = \mathbf{C} \begin{bmatrix} \hat{\boldsymbol{i}} \\ \hat{\boldsymbol{j}} \\ \hat{\boldsymbol{k}} \end{bmatrix} \tag{2.8}$$

where $\hat{\boldsymbol{i}}$, $\hat{\boldsymbol{j}}$, and $\hat{\boldsymbol{k}}$ are the unit vectors in the x-, y- and z-directions. Here the rotation matrix $\mathbf{C}(3\times 3)$, which varies both along the cable span and with time, is represented in terms of four Euler parameters $(\beta_0, \beta_1, \beta_2, \beta_3)$. Exact expressions for these are given in Tjavaras *et al.* (1998).

To derive the differential equations of motion, consider an infinitesimal segment of the cable which has an unstretched length δs, centred at a point s at a position $\boldsymbol{R}(s,t)$, as shown in figure 2. Under the applied internal and external forces and moments, the

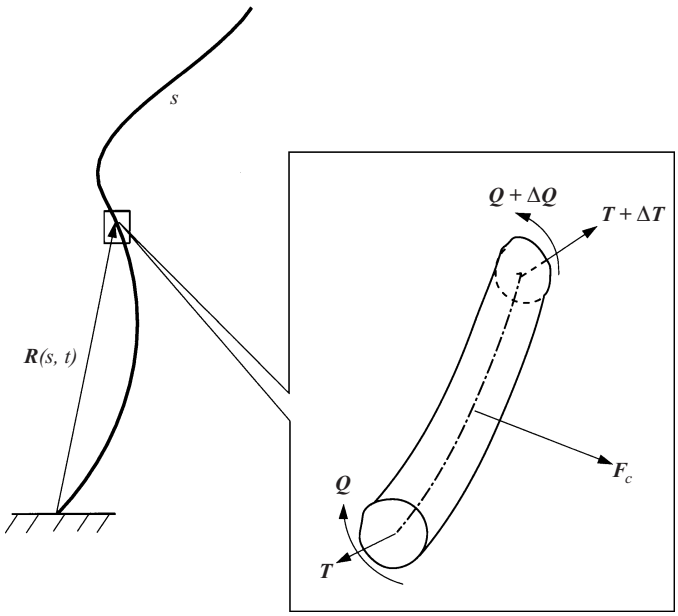

FIGURE 2. Reference system for the cable dynamics.

segment stretches to a length δs_1 and the mass per unit length of the cable segment is reduced from m_c to m_{c1}. From the conservation of mass of the cable, $m_{c1} = m_c/(1+\varepsilon)$ where the strain of the cable is $\varepsilon \equiv \delta s_1/\delta s - 1$.

The forces on the cable segment can be considered to consist of the internal force, $\boldsymbol{T} = T\hat{\boldsymbol{\tau}} + S_n\hat{\boldsymbol{n}} + S_b\hat{\boldsymbol{b}}$ where T is the effective tension in the longitudinal direction and S_n and S_b are shear forces in the transverse directions, and the external hydrodynamic force $\boldsymbol{F}_c$ (Triantafyllou 1994). Balancing these forces, we obtain

$$m_{c1}\frac{\mathrm{D}\boldsymbol{V}}{\mathrm{D}t} = \frac{\mathrm{D}\boldsymbol{T}}{\mathrm{D}s_1} + \boldsymbol{F}_c \tag{2.9}$$

where the cable velocity is $\boldsymbol{V} \equiv \partial\boldsymbol{R}/\partial t = U\hat{\boldsymbol{\tau}} + V\hat{\boldsymbol{n}} + W\hat{\boldsymbol{b}}$.

The hydrodynamic force on the cable, given by Morison's formula, takes the form

$$\begin{aligned}\frac{\boldsymbol{F}_c}{\rho} = &-\left\{\frac{\pi d C_{Dt}}{2(1+\varepsilon)^{1/2}}u_r|u_r|\right\}\hat{\boldsymbol{\tau}}\\ &-\left\{\frac{dC_{Dp}}{2(1+\varepsilon)^{1/2}}v_r(v_r^2+w_r^2)^{1/2} - \frac{\pi\rho d^2\dot{v} - 4m_a\dot{v}_r}{4\rho(1+\varepsilon)}\right\}\hat{\boldsymbol{n}}\\ &-\left\{\frac{dC_{Dp}}{2(1+\varepsilon)^{1/2}}w_r(v_r^2+w_r^2)^{1/2} - \frac{\pi\rho d^2\dot{w} - 4m_a\dot{w}_r}{4\rho(1+\varepsilon)}\right\}\hat{\boldsymbol{b}},\end{aligned} \tag{2.10}$$

where d and m_a are the diameter and the added mass (per unit length) of the cable, and C_{Dt} and C_{Dp} the drag coefficients in the tangential and normal directions. In (2.10), (u, v, w) are the fluid velocities in the (τ, n, b)-directions; and $u_r \equiv U - u$, $v_r \equiv V - v$ and $w_r \equiv W - w$ are the velocity components of the cable relative to the fluid.

Expanding the total derivative terms and making use of mass conservation, we can rewrite (2.9) in the form

$$m_c\left(\frac{\partial \boldsymbol{V}}{\partial t}+\boldsymbol{\Omega}\times\boldsymbol{V}\right)=\frac{\partial \boldsymbol{T}}{\partial s}+\boldsymbol{\Lambda}\times\boldsymbol{T}+(1+\varepsilon)\boldsymbol{F}_c, \tag{2.11}$$

where $\boldsymbol{\Omega}(s,t)$ is the angular velocity of the local Lagrangian reference frame with respect to the global Cartesian coordinate system and $\boldsymbol{\Lambda}(s,t)\equiv(\Lambda_1,\Lambda_2,\Lambda_3)$ is the Darboux vector, which is defined, as in Landau & Lifshitz (1959), to measure the material torsion of the cable but not the geometric torsion of the line. For more detailed definitions of $\boldsymbol{\Omega}$ and $\boldsymbol{\Lambda}$, see Tjavaras *et al.* (1998).

The cable is in general under the action of the internal moment $\boldsymbol{Q}=Q_\tau\hat{\boldsymbol{\tau}}+Q_n\hat{\boldsymbol{n}}+Q_b\hat{\boldsymbol{b}}$. The moment equation is given by the balance of the internal moment and the moment caused by the internal force $\boldsymbol{T}$:

$$\frac{\partial \boldsymbol{Q}}{\partial s}+\boldsymbol{\Lambda}\times\boldsymbol{Q}+(1+\varepsilon)^3\hat{\boldsymbol{\tau}}\times\boldsymbol{T}=0. \tag{2.12}$$

The components of $\boldsymbol{Q}$ follow the standard Kirchhoff assumptions on rod deformation and are given by $Q_\tau=GI_p\Lambda_1$, $Q_n=EI\Lambda_2$, and $Q_b=EI\Lambda_3$, where EI and GI_p are the bending and torsional stiffnesses of the cable, respectively.

The compatibility of the cable deformation requires that the position vector of the cable $\boldsymbol{R}(s,t)$ and its partial derivatives are continuous in both t and s. This condition leads to the following relation between the cable velocity $\boldsymbol{V}$ and the strain of the cable ε:

$$\frac{\partial \varepsilon}{\partial t}\hat{\boldsymbol{\tau}}+(1+\varepsilon)\boldsymbol{\Omega}\times\hat{\boldsymbol{\tau}}=\frac{\partial \boldsymbol{V}}{\partial s}+\boldsymbol{\Lambda}\times\boldsymbol{V}. \tag{2.13}$$

The deformation of the cable is related to the tension T by the stress–strain relation which can take the general form $T=f(\varepsilon)$ depending on the cable property. For simplicity, we adopt a linear stress–strain relation: $T=v\varepsilon$ with $v=5\times10^4$ N m^{-2}, which is a typical value for a nylon cable.

The governing equations for the cable dynamics can be summarized in a combined vector form:

$$\frac{\partial \boldsymbol{Y}}{\partial s}+\mathscr{H}(\boldsymbol{Y})\frac{\partial \boldsymbol{Y}}{\partial t}+\mathscr{P}(\boldsymbol{Y})=0, \tag{2.14}$$

where $\boldsymbol{Y}$ denotes the unknown vector

$$\boldsymbol{Y}=[\varepsilon\ S_n\ S_b\ U\ V\ W\ \beta_0\ \beta_1\ \beta_2\ \beta_3\ \Lambda_1\ \Lambda_2\ \Lambda_3]^T. \tag{2.15}$$

The coefficient matrix $\mathscr{H}$ and vector $\mathscr{P}$ are nonlinear functions of unknown $\boldsymbol{Y}$ and their exact expressions are given in Tjavaras *et al.* (1998) and are not repeated here.

For boundary conditions, at the low end of the cable the position is fixed ($\boldsymbol{V}=0$); while at the top end the position and velocity are equal to those of the centre of the buoy.

3. Numerical method

For the simulation of the nonlinear dynamics of the combined wave–buoy–cable problem, we develop a computational scheme which couples an efficient high-order spectral method for nonlinear wave–body interactions with an implicit finite-difference method for the cable dynamics. The resulting method accounts for nonlinear wave–wave and wave–body interactions up to an arbitrary high order in wave steepness and

includes the effect of vanishing tension (and bending moment) in the cable. As we shall see (see § 4), this scheme is capable of simulating highly transient snapping motion of the buoy–cable system and quantifying the resulting high-frequency free-surface signature associated with such motions.

3.1. *The high-order spectral method for wave–body interactions*

The high-order spectral (HOS) method was originally developed by Dommermuth & Yue (1987) for nonlinear wave–wave interactions and was later extended to nonlinear wave–body interactions by Liu, Dommermuth & Yue (1992) (see also Liu 1994; Liu & Yue 1998). This is a time-domain method which employs spectral representations for both the free surface and body and accounts for nonlinear wave–wave and wave–body interactions up to arbitrary order M in wave steepness. Using pseudo-spectral treatment and fast transform techniques, the method obtains exponential convergence with the number of free-surface (or body) modes and requires a computational effort which increases only linearly with the number of spectral modes and with the order M.

In terms of the surface potential $\Phi^S(x,y,t) \equiv \Phi(x,y,z=\zeta,t)$, we write the free-surface boundary conditions (2.2) in Zakharov form (Zakharov 1968):

$$\left.\begin{aligned} &\zeta_t + \nabla\zeta\cdot\nabla\Phi^S - (1+\nabla\zeta\cdot\nabla\zeta)\Phi_z(x,y,\zeta,t) = 0, \\ &\Phi^S_t + g\zeta + \tfrac{1}{2}[(\Phi^S_x)^2 + (\Phi^S_y)^2] - \tfrac{1}{2}(1+\nabla\zeta\cdot\nabla\zeta)\Phi_z^2(x,y,\zeta,t) = 0. \end{aligned}\right\} \tag{3.1}$$

These equations can be used as evolution equations for the free-surface elevation ζ, and surface potential Φ^S, provided that the free-surface velocity $\Phi_z(x,y,\zeta,t)$ can be obtained (from the boundary-value problem for Φ).

At a given time t, with known surface elevation $\zeta(x,y,t)$ and potential $\Phi^S(x,y,t)$, and position $\boldsymbol{X}(t)$ and velocity $\boldsymbol{V}_B(t)$ of the buoy, the boundary-value problem for the velocity potential $\Phi(\boldsymbol{x},t)$ is completely specified. To solve this boundary-value problem, we consider small surface wave steepness $k_I A \equiv \epsilon \ll 1$ and expand the velocity potential into a perturbation series up to order M in ϵ:

$$\Phi = \sum_{m=1}^{M} \Phi^{(m)}, \tag{3.2}$$

where $\Phi^{(m)} = O(\epsilon^m)$. We further expand the perturbation potential evaluated on the free surface $\Phi^{(m)}|_{z=\zeta}$ into Taylor series about the mean free surface $z=0$. Collecting terms at each order, we obtain a sequence of Dirichlet conditions for the perturbation potential $\Phi^{(m)}, m = 1,\ldots,M$, applied on the mean free surface:

$$\left.\begin{aligned} &\Phi^{(1)} = \Phi^S && \text{on } z=0; \\ &\Phi^{(m)} = -\sum_{l=1}^{m-1} \frac{\zeta^l}{l!}\frac{\partial^l}{\partial z^l}\Phi^{(m-l)} && \text{on } z=0, \quad m=2,3,\ldots,M. \end{aligned}\right\} \tag{3.3}$$

On the body, $S_B(t)$, the substitution of (3.2) into (2.3) leads to a sequence of Neumann conditions for $\Phi^{(m)}$:

$$\left.\begin{aligned} &\Phi^{(1)}_n = \boldsymbol{V}_B(t) && \text{on } S_B(t); \\ &\Phi^{(m)}_n = 0 && \text{on } S_B(t), \quad m=2,3,\ldots,M. \end{aligned}\right\} \tag{3.4}$$

The boundary conditions (3.3) and (3.4), along with the Laplace equation, $\nabla^2\Phi^{(m)} = 0$, and the bottom condition, $\Phi^{(m)}_z = 0$ on $z=-H$, (or for deep water $|\nabla\Phi^{(m)}| \to 0$

as $z \to -\infty$) define a sequence of boundary-value problems for the perturbation potential $\Phi^{(m)}$, $m = 1, 2, \ldots, M$, in the domain $0 \geqslant z \geqslant -H$ ($z \leqslant 0$ for deep water) and $\boldsymbol{x}$ outside the body. For calculations, we impose doubly-periodic boundary conditions at large distances $x = \pm L$ and $y = \pm L$ in the horizontal plane.

To solve the boundary-value problem at each order m, we distribute dipoles $\mu^{(m)}$ on the mean free surface and sources $\sigma^{(m)}$ on the instantaneous body $S_B(t)$. We write $\mu^{(m)}$ in a double Fourier series:

$$\mu^{(m)}(x, y, t) = \sum_p \sum_q \mu_{pq}^{(m)}(t) \mathrm{e}^{\mathrm{i}\pi(px/L + qy/L)}, \tag{3.5}$$

and $\sigma^{(m)}$ in a Chebyshev–Fourier series:

$$\sigma^{(m)}(\alpha, \varphi, t) = \sum_k \sum_\ell \sigma_{k\ell}^{(m)}(t) T_\ell(1 - 2\alpha/\pi) \mathrm{e}^{\mathrm{i}k\varphi}. \tag{3.6}$$

Here $\mu_{pq}^{(m)}$ and $\sigma_{k\ell}^{(m)}$ are the unknown modal amplitudes, α and φ are respectively the polar and azimuthal angles of a point on the body with respect to the body centre, and T_ℓ is the ℓth-order Chebyshev polynomial of the first kind. In terms of $\mu_{pq}^{(m)}$ and $\sigma_{k\ell}^{(m)}$, the perturbation potential at each order m can be expressed as

$$\Phi^{(m)}(\boldsymbol{x}, t) = \sum_p \sum_q \mu_{pq}^{(m)}(t) \Psi_{Fpq}(\boldsymbol{x}) + \sum_k \sum_\ell \sigma_{k\ell}^{(m)} \Psi_{Bk\ell}(\boldsymbol{x}), \tag{3.7}$$

where the free-surface and body basis functions $\Psi_{Fn}(\boldsymbol{x})$ and $\Psi_{Bn}(\boldsymbol{x})$ are given by

$$\Psi_{Fpq}(\boldsymbol{x}) = \int_{-L}^{L} \int_{-L}^{L} G_{z'}(\boldsymbol{x}; x', y', 0) \mathrm{e}^{\mathrm{i}\pi(px'/L + qy'/L)} \mathrm{d}x' \mathrm{d}y', \tag{3.8}$$

$$\Psi_{Bk\ell}(\boldsymbol{x}) = \int\int_{S_B} G(\boldsymbol{x}; \alpha', \varphi') T_\ell(1 - 2\alpha'/\pi) \mathrm{e}^{\mathrm{i}k\varphi'} \mathrm{d}s'. \tag{3.9}$$

In (3.8) and (3.9), G is the doubly-periodic Rankine Green function which may be represented as a doubly-infinite sum of image sources. For computations, efficient evaluation of G using summation formulas is available (Newman 1992). With the construction (3.7)–(3.9), $\Phi^{(m)}$ satisfies all the conditions of the boundary-value problem except for the boundary conditions (3.3) and (3.4) on $z = 0$ and $S_B(t)$ respectively. Substituting (3.7) into (3.3) and (3.4), the modal amplitudes $\mu_{pq}^{(m)}$ and $\sigma_{k\ell}^{(m)}$ are determined successively for $m = 1, \ldots, M$, in terms of the known free-surface elevation and potential as well as the position and velocity of the body.

After the boundary-value problems for $\Phi^{(m)}$ are solved up to the desired order M, the (total) vertical velocity on the free surface is obtained by direct differentiation and obtains the form

$$\Phi_z(x, y, \zeta, t) = \sum_{m=1}^{M} \sum_{l=0}^{M-m} \frac{\zeta^l}{l!} \frac{\partial^{l+1}}{\partial z^{l+1}} \Phi^{(m)}(x, y, 0, t). \tag{3.10}$$

Here (and in (3.3)), the first z-derivatives are obtained from (3.7) in terms of the modal amplitudes $\mu_{pq}^{(m)}$ and $\sigma_{k\ell}^{(m)}$, and all higher z-derivatives are then found using Laplace's equation: $\Phi_{zz}^{(m)} = -\Phi_{xx}^{(m)} - \Phi_{yy}^{(m)}$, $\Phi_{zzz}^{(m)} = -(\Phi_z^{(m)})_{xx} - (\Phi_z^{(m)})_{yy}$, …, and the (x, y)-derivatives are readily evaluated in spectral space.

Knowing the surface vertical velocity $\Phi_z(x, y, \zeta, t)$, the evolution equations (3.1) can be integrated in time for the new values of $\Phi^S(x, y, t + \Delta t)$ and $\zeta(x, y, t + \Delta t)$ using an

explicit scheme, say, a fourth-order Runge–Kutta scheme. Here Δt is the time step for the wave–body problem subject to a requirement for stability (see e.g. Dommermuth *et al.* 1988). The process is repeated starting from initial conditions. The potential on the body is available from (3.7) and the pressure on the body evaluated according to (2.4).

3.2. *Implicit finite-difference method for the buoy–cable dynamics*

We solve the governing differential equations for the motion of the buoy–cable system, (2.1) and (2.14), using an implicit finite-difference scheme. The discrete form of the equations is derived using the so-called box method and the resulting system of nonlinear equations is solved by iterations with relaxation (details are in Tjavaras 1996). According to Wendroff (1960), this scheme is unconditionally stable and convergent and retains second-order accuracy in space and time.

For the buoy, given its position $\boldsymbol{X}^{n-1}$ and velocity $\boldsymbol{V}_B^{n-1}$ at time t_{n-1}, we find the velocity of the buoy $\boldsymbol{V}_B^n$ at the new time, t_n, from the discrete form of (2.1):

$$\mathscr{M}\frac{\boldsymbol{V}_B^n - \boldsymbol{V}_B^{n-1}}{\delta t} = \boldsymbol{B} - \boldsymbol{W} + \boldsymbol{F}_B^{n-1/2} + \boldsymbol{T}^{n-1/2}, \tag{3.11}$$

where $t_n \equiv n\delta t$ and δt is the time step for the buoy–cable dynamics problem. The new position of the buoy $\boldsymbol{X}^n$ is obtained by integration of the buoy velocity in time:

$$\boldsymbol{X}^n = \boldsymbol{X}^{n-1} + \tfrac{1}{2}\delta t(\boldsymbol{V}_B^n + \boldsymbol{V}_B^{n-1}). \tag{3.12}$$

In (3.11), the wave force $\boldsymbol{F}_B^{n-1/2}$ is determined by extrapolation based on known previous values of $\boldsymbol{F}_B$ (obtained from the wave–body interaction problem with HOS). In the implicit scheme, the tension force $\boldsymbol{T}^{n-1/2}$ approximated by $(\boldsymbol{T}^n + \boldsymbol{T}^{n-1})/2$ is solved simultaneously with the cable dynamics problem.

For the cable, given the values of the variable $\boldsymbol{Y}_{n-1}$ at time t_{n-1}, we seek the unknown variable $\boldsymbol{Y}_n$ at time t_n from the governing equation (2.14). To do that, we divide the cable into $N_c - 1$ segments separated by N_c collocation points, $j = 1, 2, \ldots, N_c$. We write (2.14) in a discrete form at the centre of each computational 'box' formed by the time and space indices n and j. At the centre of the 'box' $(n-\frac{1}{2}, j-\frac{1}{2})$, we evaluate $\boldsymbol{Y}$ and its derivatives by

$$(\boldsymbol{Y})_{n-1/2,j-1/2} = \tfrac{1}{4}\left(\boldsymbol{Y}_{n-1,j-1} + \boldsymbol{Y}_{n-1,j} + \boldsymbol{Y}_{n,j-1} + \boldsymbol{Y}_{n,j}\right), \tag{3.13}$$

$$\left(\frac{\partial \boldsymbol{Y}}{\partial t}\right)_{n-1/2,j-1/2} = \frac{1}{2}\left(\frac{\boldsymbol{Y}_{n,j-1} - \boldsymbol{Y}_{n-1,j-1}}{\delta t} + \frac{\boldsymbol{Y}_{n,j} - \boldsymbol{Y}_{n-1,j}}{\delta t}\right), \tag{3.14}$$

$$\left(\frac{\partial \boldsymbol{Y}}{\partial s}\right)_{n-1/2,j-1/2} = \frac{1}{2}\left(\frac{\boldsymbol{Y}_{n-1,j} - \boldsymbol{Y}_{n-1,j-1}}{\delta s_{j-1}} + \frac{\boldsymbol{Y}_{n,j} - \boldsymbol{Y}_{n,j-1}}{\delta s_{j-1}}\right). \tag{3.15}$$

Here δs_{j-1} represents the unstretched length of the cable segment between the grid points $j-1$ and j. Note that δs can be different along the cable and smaller segments can be used, say, at the ends of the cable where the variations are large.

With (3.13), (3.14) and (3.15), the cable equation (2.14) can be rewritten in the discrete form

$$\begin{aligned}
&2\delta t(\boldsymbol{Y}_{n,j} - \boldsymbol{Y}_{n,j-1}) + \delta t\delta s_{j-1}(\mathscr{P}_{n,j} + \mathscr{P}_{n,j-1}) + \delta s_{j-1}(\mathscr{H}_{n,j}\boldsymbol{Y}_{n,j} + \mathscr{H}_{n,j-1}\boldsymbol{Y}_{n,j-1} \\
&\quad + \mathscr{H}_{n-1,j}\boldsymbol{Y}_{n,j} + \mathscr{H}_{n-1,j-1}\boldsymbol{Y}_{n,j-1} - \mathscr{H}_{n,j}\boldsymbol{Y}_{n-1,j} - \mathscr{H}_{n,j-1}\boldsymbol{Y}_{n-1,j-1}) \\
&= -2\delta t(\boldsymbol{Y}_{n-1,j} - \boldsymbol{Y}_{n-1,j-1}) - \delta t\delta s_{j-1}(\mathscr{P}_{n-1,j} + \mathscr{P}_{n-1,j-1}) \\
&\quad + \delta s_{j-1}(\mathscr{H}_{n-1,j}\boldsymbol{Y}_{n-1,j} + \mathscr{H}_{n-1,j-1}\boldsymbol{Y}_{n-1,j-1}), \quad j = 2, 3, \ldots, N_c.
\end{aligned} \tag{3.16}$$

Equation (3.16) together with (3.11) and (3.12) as well as the boundary conditions at the lower attachment point forms a system of $13N_c$ nonlinear equations for $13N_c$ unknowns ($\boldsymbol{Y}_{n,j}$, $j = 1, 2, \ldots, N_c$), which we solve iteratively using a relaxation method.

3.3. *Numerical implementation*

The simulation of the coupled nonlinear cable–buoy and buoy–wave interaction problem consists of three main steps. Beginning from initial values of Φ^S, ζ, $\boldsymbol{X}$ and $\boldsymbol{V}_B$, at each time t: (I) solve the boundary-value problem for $\Phi^{(m)}(\boldsymbol{x}, t)$, $m = 1, \ldots, M$, and evaluate $\Phi_z(x, y, z = \zeta, t)$ and $\boldsymbol{F}_B(t)$; (II) solve (3.16), (3.11) and (3.12) for new values of $\boldsymbol{Y}(t + \Delta t)$, $\boldsymbol{X}(t + \Delta t)$ and $\boldsymbol{V}_B(t + \Delta t)$; (III) integrate (3.1) forward in time for $\Phi^S(x, y, t + \Delta t)$ and $\zeta(x, y, t + \Delta t)$. Repeat (I)–(III) with $t + \Delta t \to t$.

Note that, in practice, the time scales of the wave–body and cable dynamics are disparate and $\delta t \ll \Delta t$ in general. Thus, step (II) above typically represents many ($\sim \Delta t/\delta t$) steps of the cable equation integration with intermediate values of F_B obtained by extrapolation of previous values of F_B given at Δt intervals.

For the wave–body problem (step I) the numbers of free-surface and body spectral modes are, in practice, truncated at suitable numbers, say N_f for Ψ_{Fpq} and N_b for $\Psi_{Bk\ell}$, and the spectral expansions in (3.5), (3.6), and (3.7) are expected to converge exponentially fast with increasing N_f and N_b. The boundary-value problems are solved using a pseudo-spectral approach, wherein all the spatial derivatives are evaluated in the spectral representation, while nonlinear products (such as those in (3.3) are computed in physical space at discrete control points. The rapid transformations between the two representations are effected by fast-Fourier transforms. (Details of the implementation can be found in Liu *et al.* 1992.)

For the overall problem, the static solution of the cable–buoy problem is chosen as the initial condition for the cable–buoy system. For incident waves, we choose exact Stokes waves (Schwartz 1974) of steepness $\epsilon = k_I A$, period τ_I and wavelength λ_I, and select a periodic domain of length and width $2L = N_w \lambda_I$, i.e. N_w complete waves in both horizontal dimensions. The far-field condition of no reflected waves is accomplished using this relatively large (doubly-)periodic computational domain. We place the buoy at the centre of the (square) domain, and, to avoid reflections for long-time simulation, we taper out the wave disturbances near the horizontal boundaries at each time step. With this tapering, the final results are unaffected when the size of the domain L is further increased (see Dommermuth & Yue 1988; Liu *et al.* 1992 for details).

3.4. *Convergence tests*

We perform systematic numerical tests to verify the accuracy and convergence of the present numerical method.

We consider a spherical buoy (diameter D) connected to the bottom (at depth $H/D = 16.7$) by a synthetic cable of unstretched length $l_0/D = 13.3$, diameter $d_0/D = 6.7 \times 10^{-3}$, and density $\rho_c/\rho = 1.11$. We consider a single incident wave, wavenumber $k_I D = 0.24$ and amplitude $k_I A = 0.13$. The sphere is given a mass of $\mathscr{M} = 0.91\rho\mathscr{V}$, i.e. 9% buoyancy. The static tension of the cable at the connection with the buoy is thus $T_s = 0.09\rho g\mathscr{V}$. Under static condition, the cable has a stretched length of $l_0 + \Delta l$ with $\Delta l \simeq 0.04 l_0$ as a result of the buoyancy of the sphere. The mean submergence of the centre of the sphere is therefore $h/D = 2.8$. For this problem, the drag coefficients set to be $C_D = 0.2$ for the sphere, and $C_{Dt} = 0.1$ and $C_{Dp} = 1.0$ for the cable.

To demonstrate convergence, we present and compare the results for the tension of the cable, T (equal to $|\boldsymbol{T}|$), at the connection point at the (centre of the) sphere.

N_f	N_b	N_c	$\Delta t/\delta t$	$M=1$	$M=2$	$M=3$
32×32	8×8	200	20	12.068	12.158	12.165
64×64	8×8	200	20	11.939	12.031	12.038
128×128	8×8	200	20	11.946	12.035	12.041
128×128	4×4	200	20	11.652	11.743	11.750
128×128	4×8	200	20	12.010	12.102	12.106
128×128	8×8	200	20	11.946	12.035	12.041
128×128	8×8	50	20	11.894	11.984	11.989
128×128	8×8	100	20	11.931	12.022	12.029
128×128	8×8	200	20	11.946	12.035	12.041
128×128	8×8	200	5	11.712	11.801	11.808
128×128	8×8	200	10	11.887	11.972	11.980
128×128	8×8	200	20	11.946	12.035	12.041

TABLE 1. Convergence of the upper-end cable tension, $T/(T_s k_I A)$, at time $t = \tau_I$ for different values of computational parameters.

For the wave–body problem itself, the convergence behaviour of the fourth-order Runge–Kutta scheme with time step Δt is well established (e.g. Dommermuth *et al.* 1988; Liu *et al.* 1992). Table 1 shows the results for T at time $t = \tau_I$ for varying perturbation order M; numbers of free-surface and body modes N_f, N_b; number of cable segments N_c; and cable integration time step δt. The computational domain is fixed at $N_w = 4$, and $\Delta t = \tau_I/50$. The exponential convergence of the results with increasing N_f, N_b and M can be observed. The expected second-order convergence rates with N_c and with δt are also obtained.

For chaotic motions (with flat power spectra), it is in general difficult to fully resolve all the spatial/temporal scales. Nevertheless, based on results such as those in table 1 and a requirement that maximum errors for the results be less than $\sim 1\%$, we use, for subsequent computations, $L = 2\lambda_I$, $N_f = 128 \times 128$, $N_b = 8 \times 8$, $N_c = 200$, and $\Delta t = \tau_I/50 = 20\delta t$. To capture the essential nonlinear wave–wave interactions, unless otherwise noted, HOS is applied with $M = 3$.

4. Numerical results

Our interest is the mechanisms for the generation of short surface waves by a submerged tethered buoy. To be specific, we consider the same cable–buoy system and configuration (including water depth and incident wavelength) as in § 3.4 and study the effects of varying incident wave amplitudes. We remark here that the physical and geometric parameters of this buoy–cable system are not atypical of such underwater moored buoys.

Even in the presence of planar incident waves, the motions of the buoy and cable may not remain planar under certain conditions (cf. Tjavaras *et al.* 1998). Although the methodology and codes of § 3 we develop are applicable for general three-dimensional motions, we assume below that the buoy–cable motions are restrained in the plane of the wave (x, z-plane). The associated free-surface disturbances are, of course, fully three-dimensional. The possible three-dimensional response of the buoy–cable is discussed in § 5 where an example is also given.

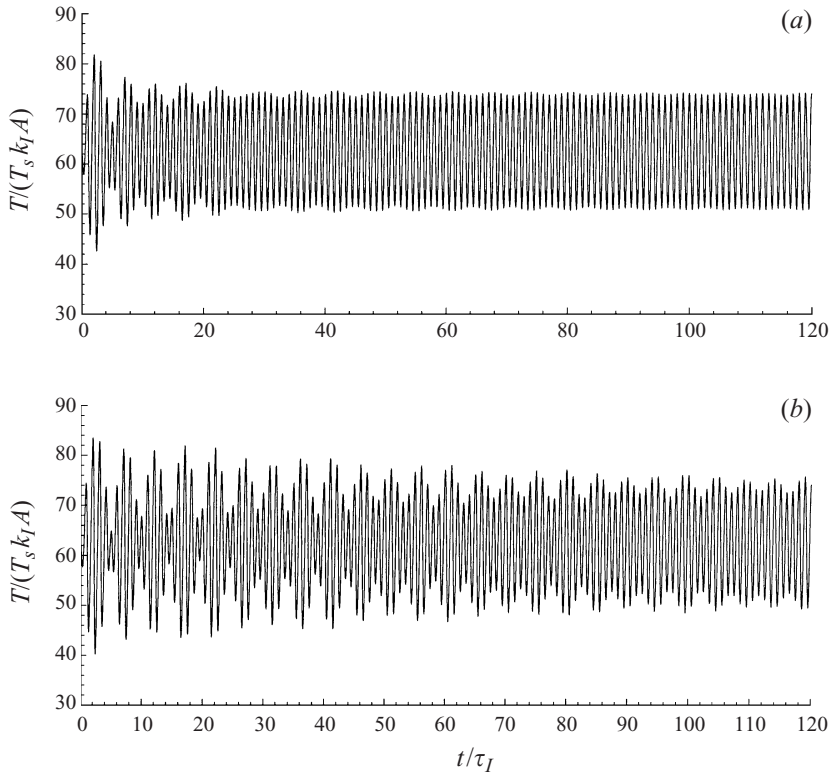

FIGURE 3. Time history of the top-end cable tension $T(t)$ for wave amplitude $k_I A = 0.016$ with hydrodynamic load on the buoy obtained using (*a*) complete wave diffraction theory (HOS, $M = 3$); and (*b*) approximation using Morison's formula (2.7) (MF).

Our simulations show that the cable motion is regular only for very small incident amplitudes (see figure 20). Beyond a threshold value in the incident wave amplitude, the buoy performs chaotic motions as a result of snapping of the tether. Such snapping motions are found to be chaotic in nature and provide an extremely effective mechanism for short-wave generation. Thus, compared to the regular motion case, the generated high-harmonic/short waves are greatly amplified once snapping motion sets in.

4.1. *Regular motion*

We consider a small incident wave amplitude corresponding to steepness $k_I A = 0.016$. Figure 3(*a*) shows the time history of the top-end cable tension. As expected for such small incident waves, the cable retains a positive tension T at all times and the cable–buoy system behaves like a (taut) inverted pendulum in oscillation. In the numerical simulations, the motion of the buoy is started abruptly from rest in an incident wave field. The tension $T(t)$ thus contains, in addition to the forcing response, a transient response associated with the abrupt start. This transient response decays exponentially with time with decay rates associated with (hydrodynamic drag and wave) damping. From figure 3(*a*), steady state (limit cycle) in T obtains after $O(30)$ incident periods. For this relatively small incident amplitude, the steady-state results exhibit very small (barely discernible) nonlinear sub/super-harmonic energy content.

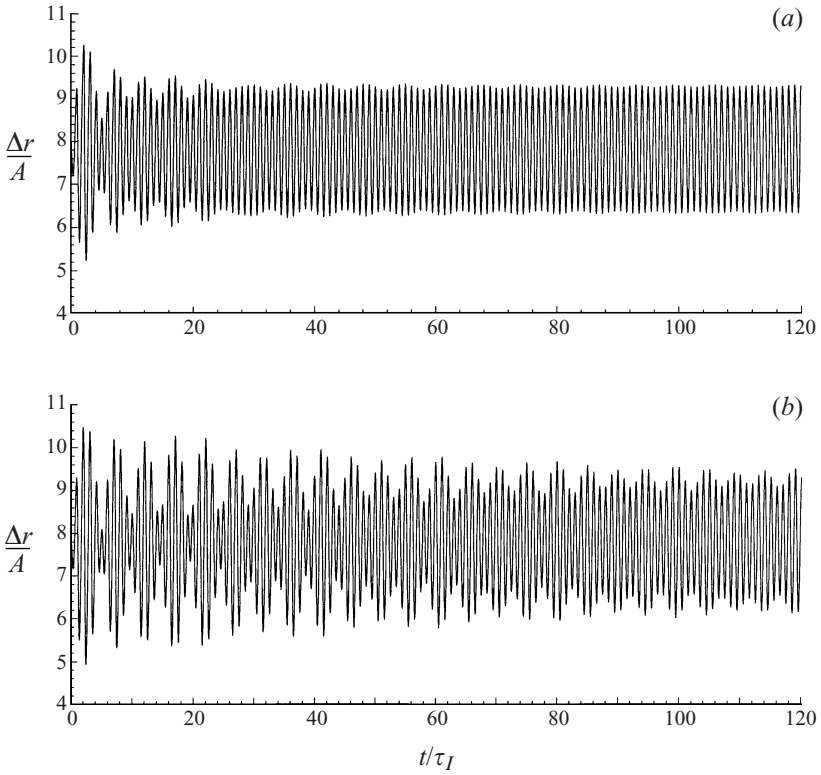

FIGURE 4. Time history of the buoy radial motion $\Delta r(t)$ for wave amplitude $k_I A = 0.016$ with hydrodynamic load on the buoy obtained using (*a*) HOS ($M = 3$); (*b*) MF.

For later reference, and also to evaluate the importance of wave scattering especially radiation damping, we obtain results for the combined wave–buoy–cable problem using a simple Morison-formula-type approximation, (2.7), instead of the nonlinear wave–body simulation using HOS. The corresponding results using (2.7) (hereafter referred to as MF as different from HOS) for the top-end cable tension T are shown in figure 3(*b*). Not surprisingly, for the relatively small buoy motions for this incident wave amplitude, the linear wave damping is much larger than quadratic viscous damping, and the start-up transients in the MF results decay unrealistically slowly. The relative magnitudes and roles of the linear wave (HOS) versus quadratic viscous (MF) damping turn out to play an important part in the *qualitatively* different behaviours of the system when the incident amplitude is increased, as we shall see in § 4.2.

The motion of the buoy in the radial direction, $\Delta r(t)$, is closely associated with the tension of the cable, which provides the restoring effect to the buoy motion. As shown in figures 4(*a*) and 4(*b*) for HOS and MF respectively, the radial buoy motion is similar to that of the top-end cable tension. As in the case of the tension, the neglect of linear wave damping leads to slow decay of initial transients although the steady states (when reached) are quite similar. Analogous results and observations are also obtained for the angular motion $\Delta\theta(t)$ of the buoy and are not presented here.

A useful way to analyse the results of figures 3 and 4, especially as a measure of the transfer of incident wave energy to high frequencies, is to obtain the frequency composition of, say, the buoy response. For the radial buoy motion, for example, the

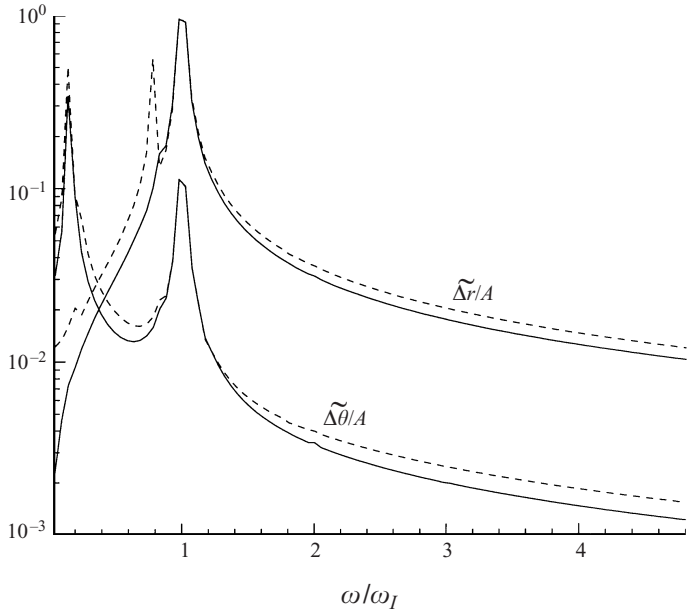

FIGURE 5. Amplitude spectra of the buoy radial and angular motions, $\widetilde{\Delta r}$ and $\widetilde{\Delta\theta}$ for wave amplitude $k_I A = 0.016$ with hydrodynamic load on the buoy obtained using: HOS ($M = 3$) (——) and MF (- - -).

value of the amplitude spectrum at frequency ω is defined by

$$\widetilde{\Delta r}(\omega) = \left| \frac{1}{n\tau_I} \int_{\tau_0}^{\tau_0 + n\tau_I} \Delta r(t) \mathrm{e}^{\mathrm{i}\omega t} \mathrm{d}t \right| . \tag{4.1}$$

Similar expressions hold for the amplitude spectra of the buoy angular motion $\widetilde{\Delta\theta}$, etc.

Figure 5 shows sample amplitude spectra for the radial and angular motions $\widetilde{\Delta r}(\omega)$ and $\widetilde{\Delta\theta}(\omega)$ (obtained using $n = 20$ and $\tau_0 = 40\tau_I$ in (4.1)). As expected, the spectra are dominated by responses at the forcing frequency, $\omega_I = 2\pi/\tau_I$, and at the (fundamental) natural frequencies in the radial (ω_{nr}) and angular ($\omega_{n\theta}$) directions respectively. These natural frequencies can be estimated theoretically or numerically. For the present system, they are respectively $\omega_{nr}/\omega_I \approx 0.8$ and $\omega_{n\theta}/\omega_I \approx 0.16$. For the radial motion, the ω_{nr} start-up transients are present in the MF approximation but are effectively damped out by wave radiation in the complete (HOS) result (cf. figure 4). For the angular motion, the fundamental natural frequency is low (wavenumber at natural frequency is $k_n D \approx 0.006$) and the wave damping at this frequency is negligibly small (according to linear theory, e.g. Newman 1993, wave damping coefficient scales as $\sim (k_n D)^3$ for $k_n D \ll 1$). The spectra using HOS and MF both exhibit the start-up transients at $\omega_{n\theta}$ and the qualitative difference between them is small.

4.2. *Chaotic motion*

In the preceding section, the wave amplitude is extremely small both in terms of wave steepness $k_I A = 0.016$, and relative to the buoy geometry: $A/D \approx 0.07$, $A/h \approx 0.02$. For somewhat increased incident amplitudes (still not large relative to steepness or geometry), it turns out the taut-inverted-pendulum-like motions of § 4.1 are no longer obtained. Instead, a complex dynamics involving vanishing tension and snapping of

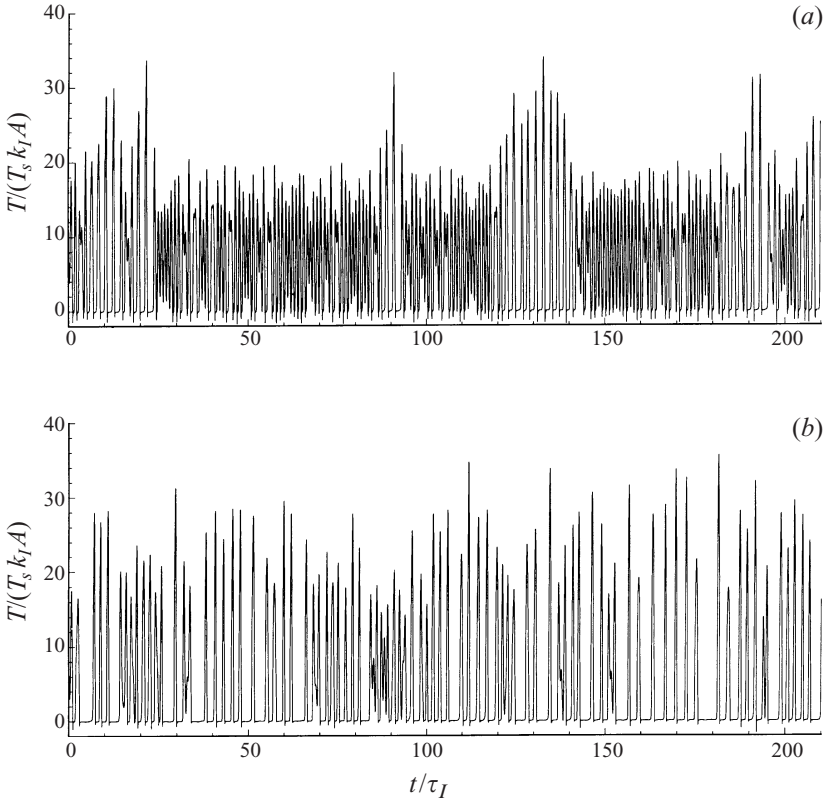

FIGURE 6. Time history of the top-end cable tension $T(t)$ for wave amplitude $k_I A = 0.13$ with hydrodynamic load on the buoy obtained using (*a*) complete wave diffraction theory (HOS, $M = 3$); and (*b*) approximation using Morison's formula (2.7) (MF).

the cable, chaotic buoy motion, and short-wave generation on the surface is found. For illustration, we consider a moderate incident wave steepness of $k_I A = 0.13$ in the following. The issue of the threshold incident amplitude for such behaviour is discussed in § 4.4.

4.2.1. *Cable snapping*

Loss of cable tension happens in a part of the motion cycle when the cable is under virtual compression due to large buoy motion along the negative (towards the anchor) tangential direction. Under these conditions, a cable without bending stiffness constitutes an ill-posed problem (Triantafyllou & Howell 1994). The inclusion of the bending terms, albeit very small, turns the problem into a well-posed one. In this case, the cable sustains a small negative tension while undergoing dynamic buckling at a (usually) high-order mode. At the opposite part of the cycle, i.e. when the buoy moves away from the anchor, there is a rapid built-up of the tension. The buoy is eventually arrested by this dynamic tension, which can become very large and impulsive in nature, constituting a so-called *cable snapping* phenomenon.

Figure 6(*a*) shows this behaviour in the top-end tension T for incident wave $k_I A = 0.13$. The time history shows periods when $T(t)$ is zero or (slightly) negative, separated by sharp spikes. The durations of these low-tension periods and spikes, as well as the amplitudes of the spikes, are quite irregular. The irregular motion itself

appears to switch between two different modes both of which are dominated by cable snapping. The two modes differ qualitatively in terms of the 'average' peak amplitude and the 'average' period between snapping spikes. Referring to figure 6(*a*) (see also figure 7*a*), we identify the two modes: mode A (e.g. for $t/\tau_I \lesssim 25$, $\sim 85 < t/\tau_I \lesssim 95$, etc.) characterized by larger average peak amplitude and lower average snapping frequency; and mode B (e.g. for $\sim 25 < t/\tau_I \lesssim 85$, $\sim 95 < t/\tau_I \lesssim 120$, etc.) characterized by lower peak amplitudes and higher frequencies. A more careful examination (see also figure 8 for the spectra) reveals that the snapping frequency for mode B is close to that of the incident wave, while mode A is approximately a sub-harmonic with characteristic frequency half that of ω_I.

If wave damping effect is ignored, figure 6(*b*), the MF approximation prediction again shows the irregular behaviour but now without the switching of modes (with mode B effectively absent). Thus, the presence of a linear damping by wave radiation appears to be necessary for the appearance of two competing chaotic modes.

4.2.2. *Buoy motion*

We will find that the motion corresponding to figure 6 is in fact chaotic. Indeed, the characteristic behaviour is qualitatively similar to that of the so-called 'bouncing-ball' problem (Shaw 1985), namely the bouncing motion of an elastic ball confined in an oscillating closed box. Our numerical simulations reveal that the mechanism of chaotic motion of the buoy constrained by a snapping cable is as follows: (*a*) at some time, as a result of wave excitation on the buoy, the total tension of the cable drops to zero or (slightly) negative while the compressing motion of the buoy continues; (*b*) in the absence of tension, the collapsing cable undergoes a classical buckling instability; (*c*) some time later, as the cable is reloaded by the wave force on the buoy, the cable tension rises rapidly. The direction of the tension in (*c*) depends on the precise orientation of the cable at its connection with the buoy at the instant the spike-like tension is applied. Due to the instability in (*b*), this dependence is unpredictable and extremely sensitive. Note that the timing of (*c*) (as well as (*a*)) depends on the wave exciting force (amplitude and direction) on the buoy, which in turn is a function of the (chaotic) motion (history) of the buoy, and hence is itself chaotic.

Figure 7 shows time histories of the radial motion of the buoy $\Delta r(t)$ with HOS ($M = 3$) and with the MF approximation. The time behaviours are similar to T (figure 6). For the result with nonlinear wave diffraction, figure 7(*a*), the switching between two competing chaotic modes (A of relatively larger amplitude and longer characteristic period than B) is even more evident here for the radial motion than in figure 6(*a*).

Frequency analyses of $\Delta r(t)$ in figure 7(*a*) is presented in figure 8. By selecting the initial time τ_0 in (4.1), we are able to obtain the characteristic amplitude spectra for modes A and B separately. Unlike the regular motion case (cf. figure 5), the amplitude spectra in the present case are broad band with slow decay with increasing frequency for large frequency. Such spectra indicate that the radial buoy motion is chaotic. Comparing modes A and B, figure 8 shows that mode A has greater total energy and with almost all of the added energy concentrated at low frequencies. The peak energy of mode B appears near the incident frequency while that of mode A appears to be at a first sub-harmonic ($\omega/\omega_I \approx 0.5$). These support the observations based on figures 6(*a*) and 7(*a*).

Results for the angular motion are qualitatively similar to those for the radial motion presented here and are not repeated.

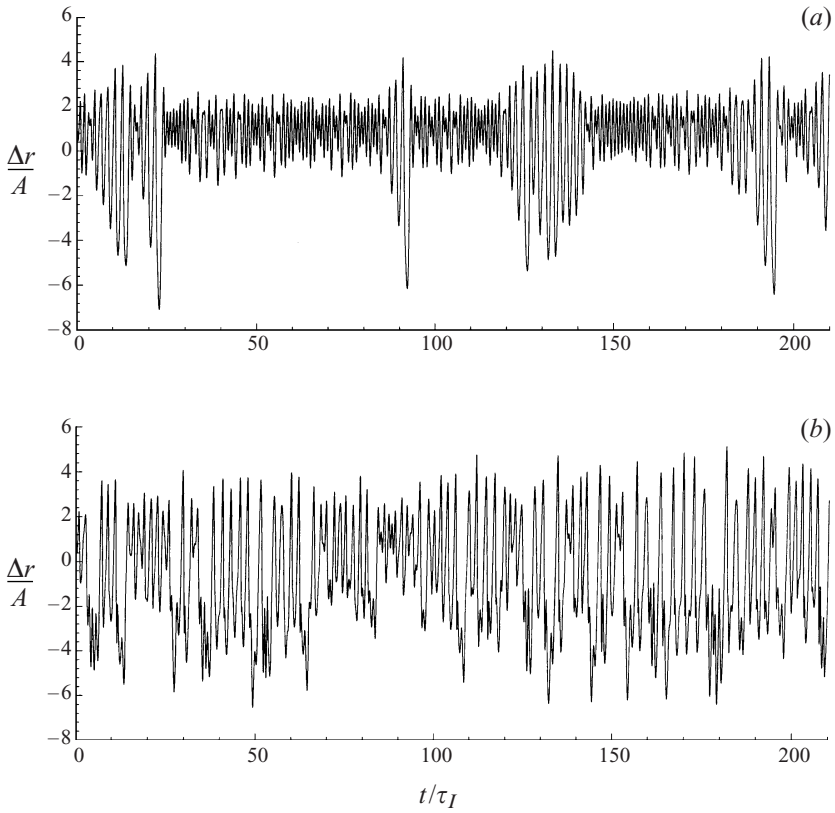

FIGURE 7. Time history of the radial motion of the buoy for $k_I A = 0.13$ with the hydrodynamic load on the buoy obtained using (*a*) HOS ($M = 3$); and (*b*) MF.

4.2.3. *Lyapunov exponents*

An essential characteristic of chaos is the exponential sensitivity to initial conditions. For a chaotic motion, two trajectories with slightly different initial conditions can be expected to diverge exponentially in time. This feature can be measured by the so-called Lyapunov exponent.

Beginning with a reference trajectory and a neighbouring trajectory, if the motion is chaotic and the two trajectories diverge exponentially with time, we have

$$\delta \propto 2^{\sigma t/\tau_I}, \tag{4.2}$$

where δ is the distance between the two trajectories, and the dimensionless parameter σ is the Lyapunov exponent. A positive value of the Lyapunov exponent is indicative of chaos. To obtain the maximum Lyapunov exponent σ_m in the present case, we apply the method of Wolf *et al.* (1995) which involves the reconstruction of pseudo-phase space from time-history data. Figure 9 displays the time variations of the Lyapunov exponents for the HOS and the MF results. In both cases, asymptotic positive Lyapunov exponents are obtained for large time. For comparison, the result for the small incident wave case of § 4.1 is also plotted. As expected, for this regular motion, the value of the Lyapunov exponent approaches zero as time increases.

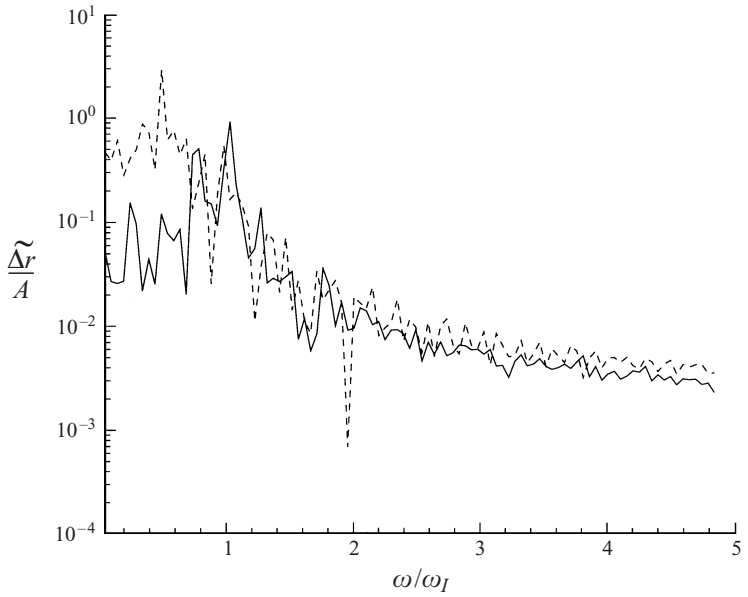

FIGURE 8. Amplitude spectra of the radial motion of the buoy for $k_I A = 0.13$ obtained with HOS ($M = 3$). The results plotted are for modes: A (- - -, obtained using $\tau_0 = 150\tau_I$, $n = 20$ in (4.1)); and B (——, $\tau_0 = 120\tau_I$, $n = 20$).

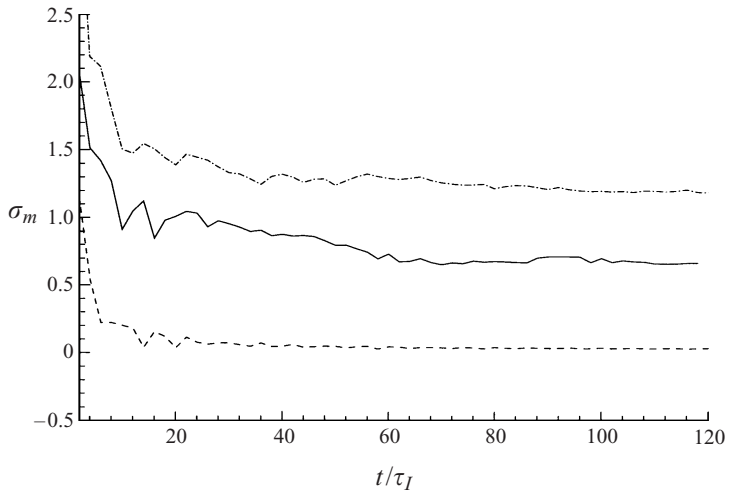

FIGURE 9. Variations of the maximum Lyapunov exponent σ_m as a function of time. The results shown are for $k_I A = 0.13$ obtained using: HOS ($M = 3$) (——) and MF (— · —) and for $k_I A = 0.016$ obtained using HOS ($M = 3$) (- - -).

From figure 9, we also observe that the Lyapunov exponent for HOS is smaller than that for the approximate MF solution. This can be expected since HOS accounts for the effect of wave damping which reduces the extent of chaos.

4.2.4. *Poincaré sections*

The global behaviour of the buoy–cable system is elucidated by examining the Poincaré sections of the motions in phase space. Figure 10 shows the Poincaré map in

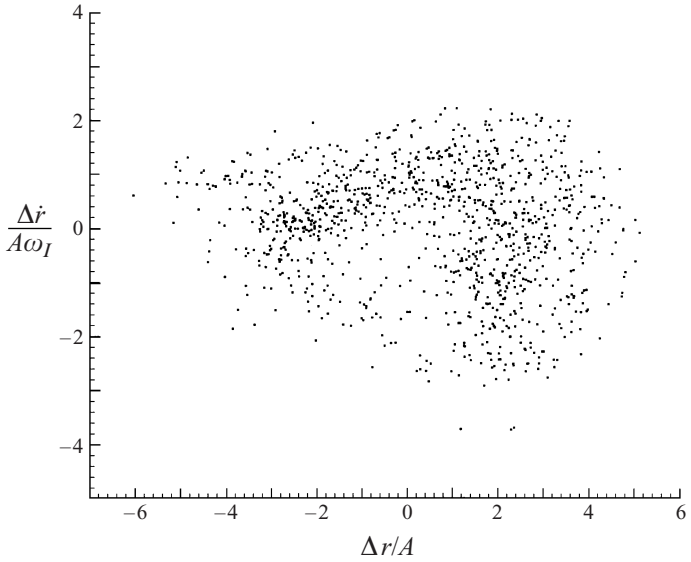

FIGURE 10. Poincaré map of the radial motion of the buoy for $k_I A = 0.13$ obtained using HOS ($M = 3$).

the buoy radial displacement–velocity plane for $O(200)$ periods τ_I. The points appear to fill a region and indicate chaotic orbits.

Assuming planar motion (see § 5), the complete Poincaré section of the buoy motion represents a surface in four-dimensional space. Its projection onto a two-dimensional plane such as the one in figure 10 does not therefore reveal a clear fractal structure (see e.g. Moon 1992).

To obtain a Poincaré section showing the fractal structure, we consider a reduced model of the problem by restraining the buoy motion to the radial direction only (neglecting any coupling with the angular motion). The equation of motion (2.1) then reduces to a simpler form (a piecewise linear dynamic system, see e.g. Holmes 1982) for the radial motion $r(t)$:

$$\ddot{r} + b\dot{r} + cr = (f \sin \omega t + a)/(\mathscr{M} + \mathscr{M}_a). \tag{4.3}$$

The effect of wave damping is included in (4.3) using a linear damping term $b\dot{r}$, where b is a constant. To account for the cable snapping effect, we employ a restoring force cr with $c = \omega_{nr}^2$ for $r \geqslant l_0$, and $c = 0$ otherwise, i.e. the restoring force is present only when the cable is stretched. In (4.3), $f \sin \omega t$ represents the incident wave excitation and $a = 0.09\rho g \mathscr{V}$ is the net buoyancy of the sphere.

Starting with initial conditions, (4.3) can be integrated forward in time to obtain the time history $r(t)$. Using the model represented by (4.3), we are able to show that there exists a threshold value of the excitation amplitude of f below which the motion is regular and above which the motion is chaotic. Figure 11 shows a sample result for $r(t)$. The time history again displays the characteristic chaotic behaviour and significantly also the switching between two competing A-, B-like modes.

Figure 12(a) shows a Poincaré plot in the $(r, \dot{r})$-plane for $O(20\,000)$ periods of (4.3). The points fill a region with a rich fractal structure. The presence of two (main) competing modes can be elucidated by plotting the contributions to figure 12(a) from modes A and B (defined, say, by negative peak amplitudes greater than r_A for mode

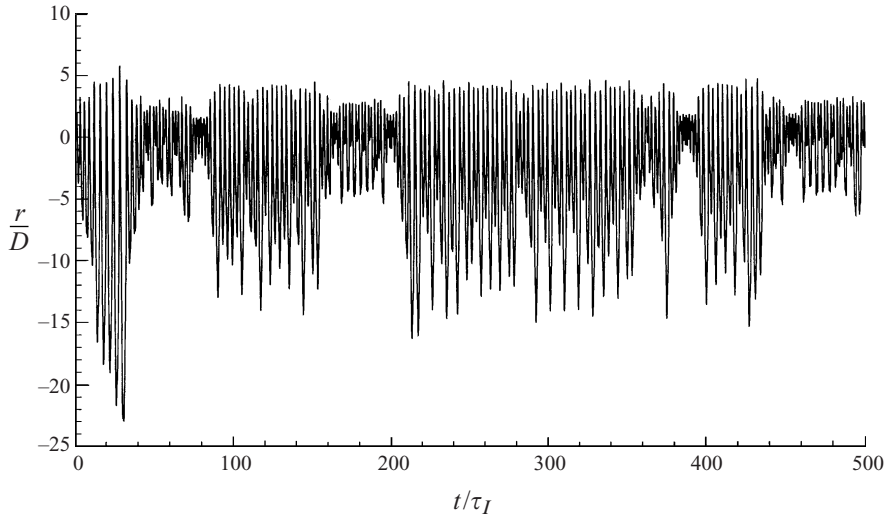

FIGURE 11. Time history of the radial motion $r(t)$ based on the reduced model (4.3) with $b = 0.015\omega_{nr}$ and $f = D\omega_{nr}^2$.

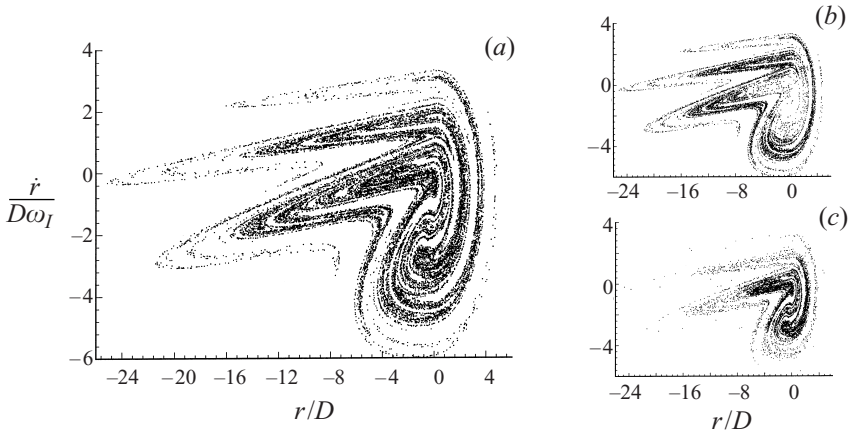

FIGURE 12. Poincaré maps based on (4.3) with $b = 0.015\omega_{nr}$ and $f = D\omega_{nr}^2$ for: (*a*) the total motion; (*b*) mode A only; and (*c*) mode B only.

A and mode B otherwise). These are shown in figures 12(*b*) and 12(*c*) for $r_A = -5$. Thus the total Poincaré section appears to contain two main regions of attraction, one (corresponding to mode A) lying outside another (corresponding to B). Figure 12 shows substantially more details such as fingering than figure 10 for the full system. This is primarily due to the fact that the full system has more (two versus one) degrees of freedom and the projection of its four-dimensional Poincaré map onto two dimensions only partly reveals the full fractal structure.

4.3. *Free-surface pattern*

A motivation for this work is to obtain the free-surface disturbance above a buoy–cable system such as the one we consider in the presence of ambient waves. Of particular interest are the pattern and amplitudes, especially for short waves. In view of the qualitatively different buoy–cable behaviours observed in the preceding

sections, the free-surface disturbances are expected to be quite different depending on whether the buoy–cable motions are regular (very small incident wave amplitude, no cable snapping) or chaotic (moderate incident amplitude, cable snapping). Since the MF approximation does not account for the wave diffraction/radiation effects, the results presented here are all obtained using HOS ($M = 3$). Note that for clarity, in all the following results for the surface elevation and spectrum, the contribution of the incident wave itself is subtracted.

For sufficiently small incident amplitude, the buoy–cable motion is a regular periodic oscillation (cf. figure 3). The period of the buoy response is equal to that of the incident wave and the response amplitude is, in general, comparable to that of the incident wave. In this case, the free surface contains high-harmonic/short waves as a result of non-linear wave–wave and wave–body interactions. The mth-harmonic wave, $m = 1, 2, \ldots$, has frequency $m\omega_I$ and has (free-wave) wavelength of λ_I/m^2, while its amplitude scales as $O(\epsilon^m)$, in general.

For somewhat larger incident wave amplitude, the buoy–cable motion is no longer regular/periodic, the overall dynamics is dominated by cable snapping and the response is chaotic (cf. figures 6, 7). The frequency of the buoy response is broad band (figure 8) and so also the resulting surface wave disturbance. This turns out to be a remarkably effective mechanism for transferring energy from the incident wave to high-frequency short waves.

4.3.1. *Surface elevation*

Figure 13 shows the time evolution of the free-surface elevation above the initial (rest) position of the buoy for $k_I A = 0.016$ and $k_I A = 0.13$. For the small-amplitude ($k_I A = 0.016$) case, figure 13(a), a constant-amplitude (periodic at frequency ω_I) steady state is quickly reached after initial transients vanish. The diffracted/radiated wave amplitude in this case is only approximately 1% that of the incident wave. The diffracted/radiated wave elevation over the buoy for the larger incident wave amplitude ($k_I A = 0.13$) is plotted in figure 13(b) using the same scales. Not surprisingly, the chaotic buoy motion produces an irregular free-surface elevation characterized by the presence of substantial high-frequency content, and an order-of-magnitude greater normalized (by incident amplitude) peak amplitudes.

The presence of two underlying modes of motion can also be discerned from figure 13(b). The large-amplitude peaks in the surface elevation are associated with and are precursors to the transitions from mode A to mode B. Since the (average) kinetic energy of the buoy is higher in mode A than in mode B, the difference in that energy is released to the free surface in the switching of the buoy motion from A to B. This explains why in the MF simulations, mode B is never established in the absence of this energy transfer mechanism.

Figure 14 shows the differences between the centreline ($y = 0$) free-surface profiles for $k_I A = 0.016$ versus 0.13. The instantaneous profiles are taken at the same time, $t/\tau_I = 23$, which corresponds to an instant just after a sudden release of energy in a mode A to mode B transition by the buoy. Comparing the two profiles, the substantial presence of short waves and overall larger normalized amplitude of the radiated/diffracted waves as a result of snapping-induced chaotic motion of the buoy are evident.

The three-dimensional wave pattern over the buoy is also of interest. Figure 15 shows sample free-surface snapshots at the same time instant $t = 23\tau_I$ for regular and chaotic buoy motions. For regular buoy motion, the buoy dynamics is dominated by radial r (heave) rather than angular θ (surge) motions in this case and the

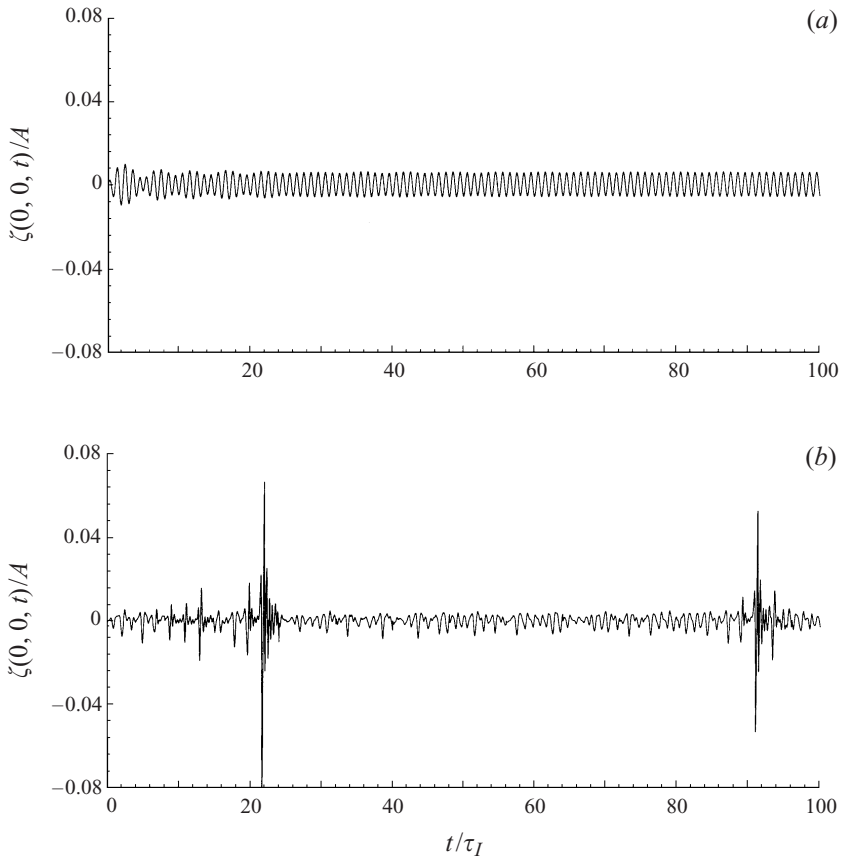

FIGURE 13. Time evolution of the free-surface elevation above the initial (rest) position of the buoy for incident wave steepness (*a*) $k_I A = 0.016$; and (*b*) $k_I A = 0.13$. The incident wave itself is subtracted.

free-surface elevation is approximately axisymmetric (figure 15*a*). The overall pattern is thus roughly that due to a submerged vertical dipole of periodic strength. The surface pattern associated with snapping chaotic motion, figure 15(*b*), is much more interesting. The radiated/diffracted waves are now outweighed by short waves both radially and circumferentially. The wavefield is now not axisymmetric but somewhat dipole-like indicative of large surge motions of the buoy. From figure 15, it is also seen that the overall normalized wave amplitudes are substantially greater for irregular motion.

4.3.2. *Spectra of the free-surface disturbance*

From the point of view of remote observation, the wavenumber (and frequency) spectra of the three-dimensional free-surface elevation as well as of the surface slope are often of importance.

We first consider the time variation of the surface elevation $\zeta(0, 0, t)$ directly over the (rest position of the) centre of the buoy. Figure 16 shows the frequency amplitude spectrum of this elevation (shown in figure 13) for the two wave amplitude cases we consider. For small incident amplitude ($k_I A = 0.016$), the spectral amplitude is dominated by that at the incident frequency ω_I. This is evident from the wave

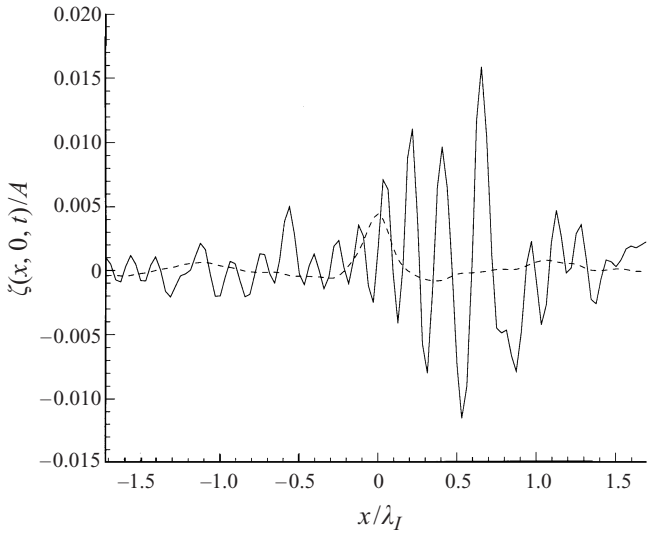

FIGURE 14. Free-surface wave profiles on $y = 0$ at time $t/\tau_I = 23$ for: $k_I A = 0.13$ (——) and $k_I A = 0.016$ (- - -). The incident wave itself is subtracted.

elevation history (figure 13) and is consistent with the frequency spectrum of the buoy motion (figure 5).

For $k_I A = 0.13$, the surface amplitude spectrum shows broad-band features similar to those of the buoy motion amplitude spectrum. It is noteworthy that the spectrum for $\zeta(0, 0, t)$ is in fact appreciably broader than that for $\Delta r(t)$. The reason is associated with the continuous spectrum of the free surface due to a submerged transient source (cf. e.g. Wehausen & Laitone 1960, § 13γ). In terms of the broad-band response, the wave disturbance can be considered to be in some sense more irregular or chaotic than the underlying buoy motion. Thus the present system provides a very effective mechanism of energy transfer from ω_I to multiple (short-wave) frequencies.

The short-wave content of the free-surface disturbance can be seen even more clearly in its wavenumber spectrum. For clarity, we consider first the surface elevation along the x-axis (cf. figure 14). Figure 17 plots the one-dimensional wavenumber (k_x) amplitude spectra for $\zeta(x, 0, t)$ for regular and chaotic motions (normalized by incident amplitude A). As expected, the spectral peak is at $k_x/k_I = 1$ for regular motion ($k_I A = 0.016$). For the chaotic case, the wavenumber spectrum is almost constant with no apparent decrease at least up to $k_x/k_I \gtrsim 8$ (this value being limited by the spatial resolution of HOS). Comparing the two amplitude spectra, it is seen that the (normalized) wave amplitude for chaotic motion can be two or more orders of magnitude greater than that for regular motion for large k_x/k_I.

A more complete picture of the spectral content of the wave pattern is obtained by plotting the two-dimensional wavenumber k_x, k_y amplitude spectra of the free-surface elevation (shown in figure 15). These are displayed as contour (grey-scale) plots in figure 18. For the regular motion case ($k_I A = 0.016$), figure 18(a), the two-dimensional spectrum is approximately axisymmetric consistent with underlying buoy motions dominated by heave (radial motion) (cf. figure 15a). The diffracted/radiated wave energy is centred around the incident wavenumber, $k_x^2 + k_y^2 = k_I^2$, while small amounts of energy (vaguely visible in the plot) can be found at higher harmonics as a result of nonlinear interactions.

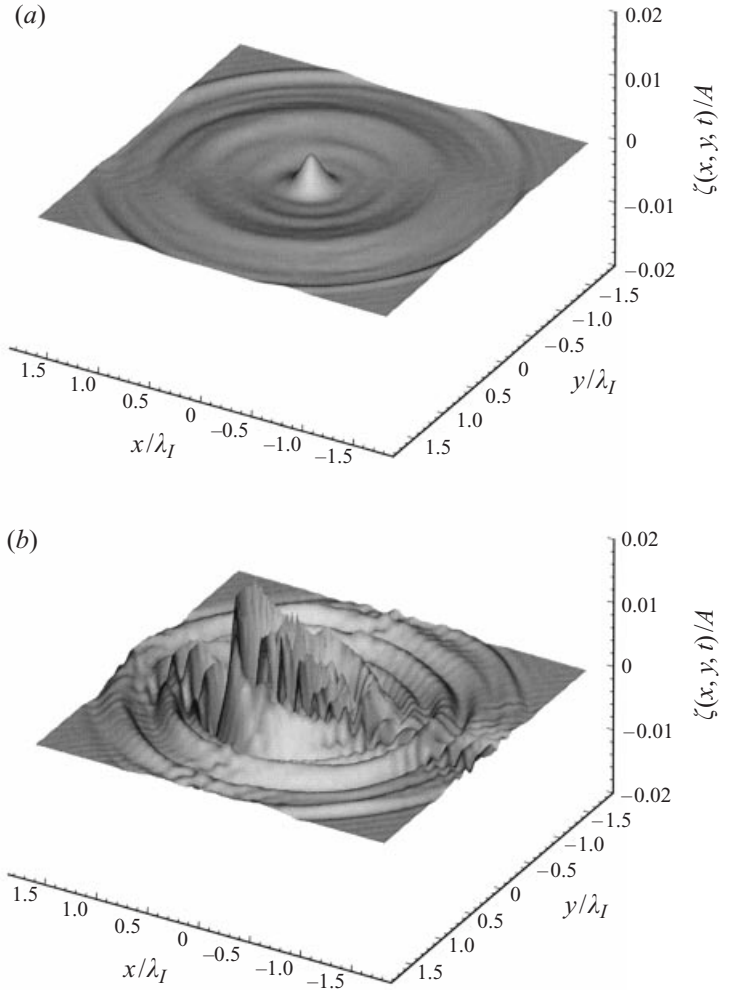

FIGURE 15. Instantaneous three-dimensional free-surface wave elevation (normalized by A) at time $t/\tau_I = 23$ for: (*a*) $k_I A = 0.016$; and (*b*) $k_I A = 0.13$. The incident wave itself is subtracted. Note that the vertical scales are the same.

For larger incident wave amplitude, $k_I A = 0.13$, the spectrum associated with chaotic motion is dramatically different. Substantial amounts of wave energy from the incident wavenumber is spread into high wavenumbers. With the exception of several ring-like lighter bands, the spectral amplitude is appreciable in the entire two-dimensional wavenumber space (cf. e.g. figure 17). Also unlike the regular motion case (figure 18*a*), the two-dimensional spectrum for the chaotic motion is not completely axisymmetric, but with somewhat more of diffracted/radiated wave energy in the low $|k_y|$ wave-numbers. This is consistent with the observation of a non-axisymmetric wave pattern (see figure 15*b*) and the presence of appreciable surge motions of the buoy.

Finally, we show, in figure 19, the one-dimensional scalar wavenumber $\kappa \equiv (k_x^2 + k_y^2)^{1/2}$ spectra of the two-dimensional free-surface elevation for regular and chaotic motions. Overall, the spectra behave similarly to the one-dimensional (k_x) spectra of the wave profile on $y = 0$ (cf. figure 17). For the regular motion case, $k_I A = 0.016$, the

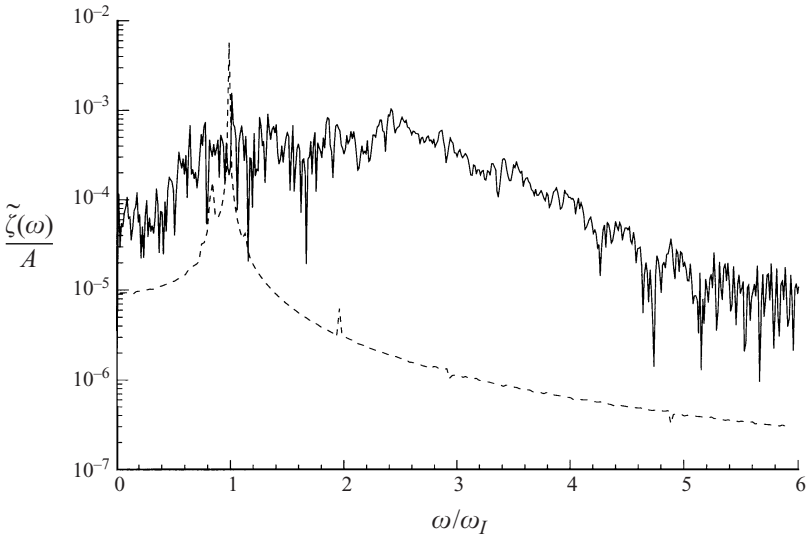

FIGURE 16. Amplitude spectra of the free-surface elevation above the initial (rest) position of the buoy for incident wave steepness: $k_I A = 0.13$, ——; and $k_I A = 0.016$, - - -. The incident wave itself is subtracted.

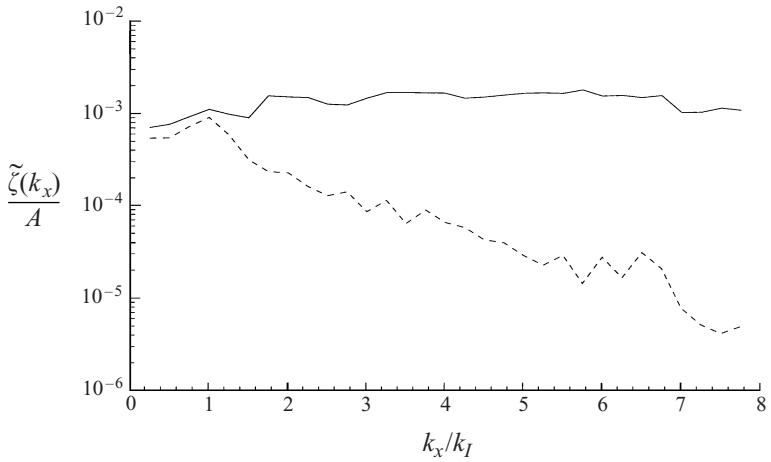

FIGURE 17. Wavenumber amplitude spectra of the free-surface wave elevation on $y = 0$ for: $k_I A = 0.13$ (——) and $k_I A = 0.016$ (- - -). The incident wave itself is subtracted and the spectra are averaged over three incident periods around $t/\tau_I = 23$.

diffracted/radiated wave energy is concentrated at the incident wavenumber $\kappa = k_I$ and vanishes as the wavenumber κ increases. For chaotic motions, $k_I A = 0.13$, the amplitude of the spectrum is nearly constant at least up to $\kappa/k_I \gtrsim 8$. Not surprisingly, at larger wavenumbers, the spectral amplitude can be two or more orders of magnitude greater than that for regular motions.

These results demonstrate the effectiveness of a submerged tethered buoy in transferring incident wave energy to high wavenumbers and frequencies. Relative to classical mechanisms of nonlinear wave–body interactions, the efficacy of cable snapping and subsequent chaotic motion for short surface wave generation is truly remarkable.

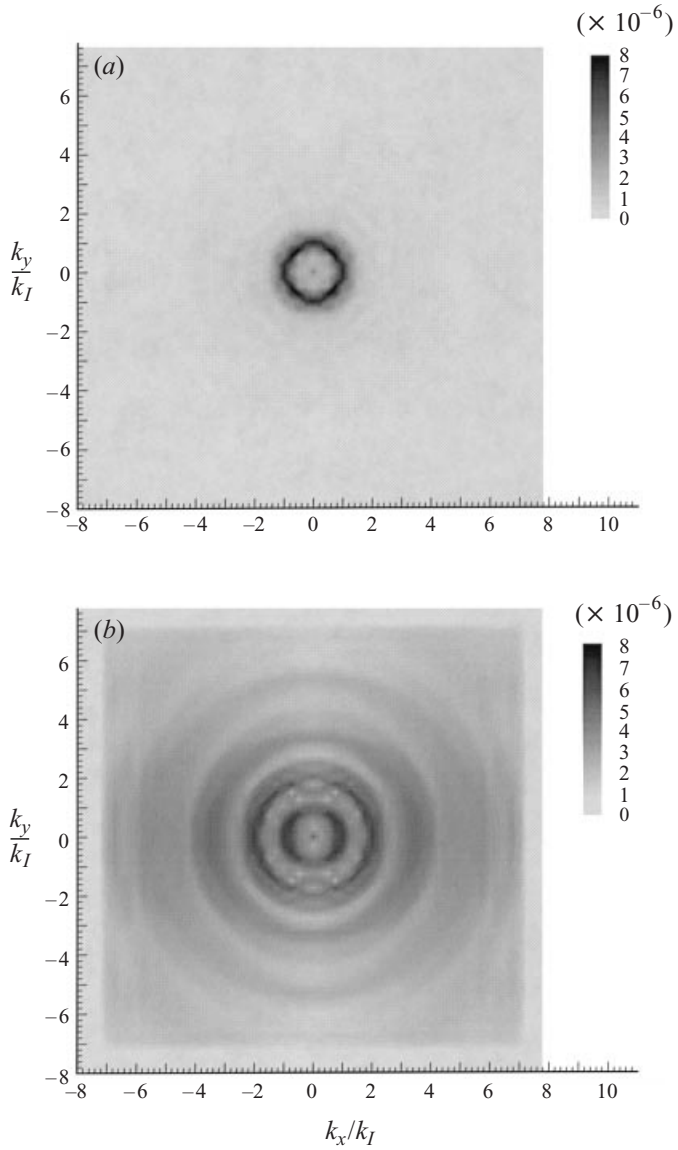

FIGURE 18. Two-dimensional wavenumber amplitude spectra of the free-surface wave elevation for: (*a*) $k_I A = 0.016$; and (*b*) $k_I A = 0.13$. The incident wave itself is subtracted and the spectra are averaged over three incident periods around $t/\tau_I = 23$.

4.4. *Criterion for the onset of chaos*

The chaotic response of the tethered buoy under incident waves results from the snapping of the cable. The snapping occurs whenever the tension in the cable is lost in compression and is then regained rapidly. Based on this physical understanding, it is possible to obtain a threshold value for the body motion amplitude above which the cable will lose its tension at least for a part of the motion cycle. Since the body motion is wave driven, this in turn provides a criterion for the onset of cable-snapping and chaotic response in terms of a threshold incident wave amplitude.

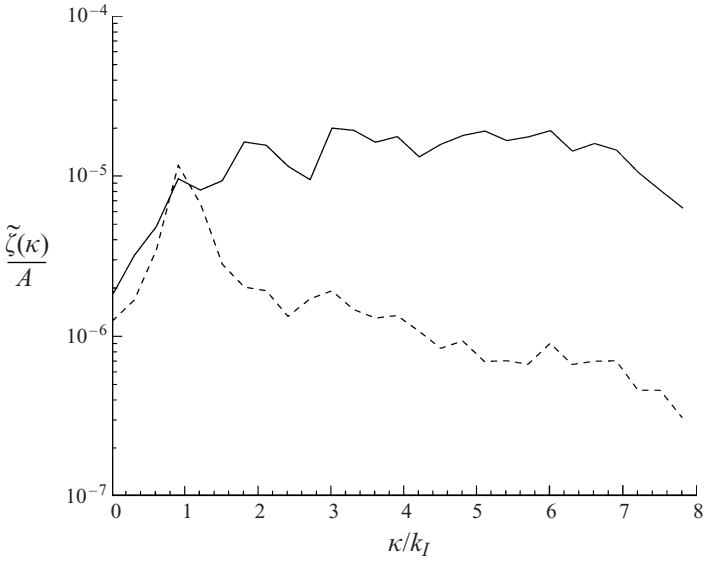

FIGURE 19. One-dimensional scalar wavenumber amplitude spectra of the free-surface wave elevation for: $k_I A = 0.13$ (——) and $k_I A = 0.016$ (- - -). The incident wave itself is subtracted and the spectra are averaged over three incident periods around $t/\tau_I = 23$.

In general, this criterion for the onset of chaos in terms of incident wave amplitude depends on the incident wavelength, the body geometry and submergence, and the cable geometry and properties. For a given cable–buoy configuration/property, the dependence of the threshold wave amplitude on the incident wavelength can be obtained qualitatively. When the incident frequency is close to the natural frequencies of the cable–buoy system, the response of the body is amplified and cable snapping is obtained for smaller incident wave amplitudes. In the limit of low wave frequency, the body moves with the fluid particles and cable snapping would occur when the incident wave amplitude exceeds the static extension of the cable. In the other limit, when wave frequency is high (relative to submergence/gravity), wave excitation is rapidly attenuated and chaotic body response does not occur.

Such a criterion for onset of chaotic motions can also be obtained directly by simulations. Figure 20 shows such results obtained by numerical simulations using HOS varying $k_I A$ for a wide range of ω_I/ω_{nr} (ω_{nr} is the fundamental natural frequency of the buoy–cable in the radial direction). The behaviour supports well that based on physical arguments above. Note that in figure 20, the appearance of a dip near $\omega_i/\omega_{nr} \sim 0.5$ is a result of nonlinear (second-order) double-frequency wave excitation.

From figure 20, we also conclude that for reasonably large incident amplitudes, cable snapping and chaotic motions occur over a broad frequency band. While figure 20 is obtained for a specific buoy–cable configuration, our numerical experiments confirm that snapping/chaotic motion is a common phenomenon for a wide range of physical and geometric parameters of such systems.

5. Discussion

In this paper, we study the coupled nonlinear dynamics of a submerged tethered buoy in waves. Of interest are the resulting buoy motions, the associated free-surface disturbance, and, in particular, nonlinear mechanisms for short surface wave

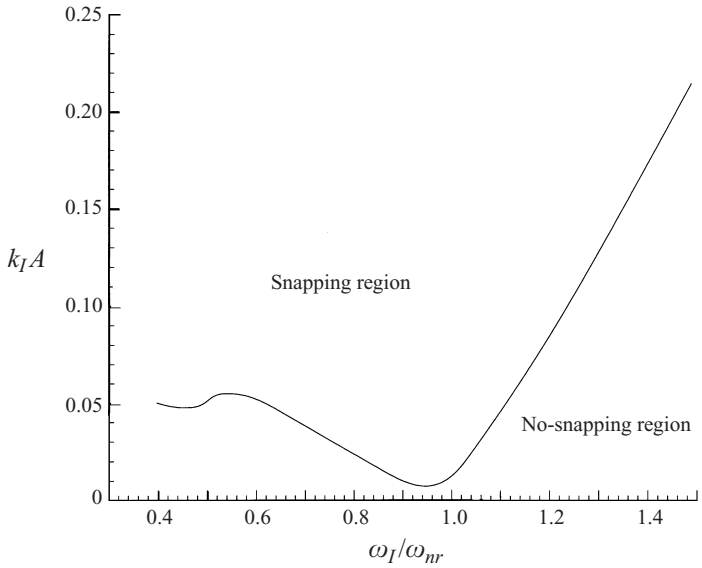

FIGURE 20. Threshold value of the incident wave steepness as a function of wave frequency (relative to natural heave frequency of the buoy–cable system) for the occurrence of cable snapping.

generation. We develop effective simulations of this problem by combining a robust cable dynamics program (capable of modelling loss of tension and snapping) and a high-order spectral method for the nonlinear wave–wave, wave–body interactions.

For demonstration, we choose a specific but typical buoy–cable system and incident wavelength. Our numerical simulations show that for incident wave amplitudes above some threshold value (depending on the buoy–cable configuration and wave frequency), snapping of the cable occurs. The resulting buoy motions and the associated surface disturbance then exhibit chaotic behaviours which we study using standard methods. Of particular note in the chaotic dynamics is the switching between two distinct chaotic snapping modes which occurs only when wave radiation damping is accounted for. Analyses of the three-dimensional free-surface patterns and their frequency and wave-number spectra reveal that cable snapping and chaotic buoy motions provide a remarkably effective mechanism for transferring energy from the incident wave to high-frequency short waves. Such a mechanism can be several orders of magnitude more effective than that due to nonlinear wave–body interactions alone in the absence of cable snapping.

Finally we remark on the assumption of planar motion of the buoy–cable system in this work. For a planar incident wave, it has been shown that the buoy–cable motion remains planar in the absence of cable snapping; but, not surprisingly, is unstable to small out-of-plane disturbances when cable snapping and chaotic motions are present (Tjavaras *et al.* 1998). Figure 21 shows a sample trajectory, projected onto the horizontal (x, y)-plane, of a buoy under snapping/chaotic conditions but now given a small initial displacement from the vertical symmetry (x, z)-plane. The three-dimensional nature of the ensuing buoy motions is evident. In addition to such planar instability effects, three-dimensional motions can also result from out-of-plane forcing such as currents and non-symmetric vortex shedding. The coupled nonlinear/chaotic dynamics involving three-dimensional buoy–cable motions is quite complex and is the subject of current investigation.

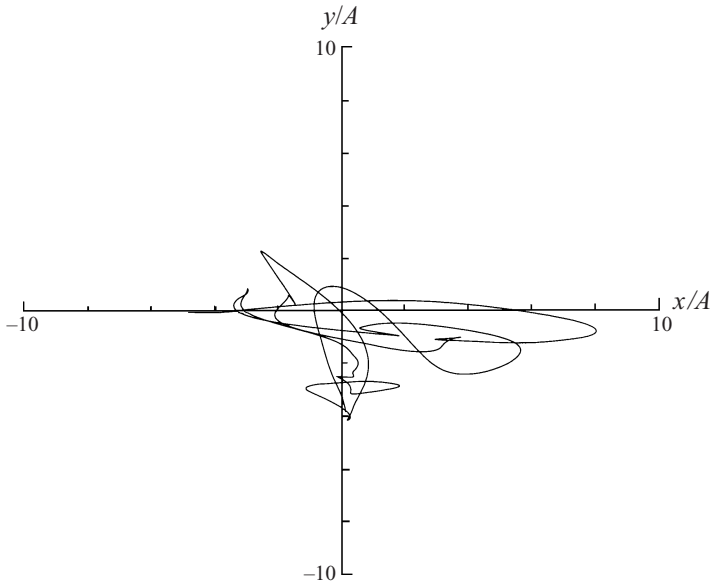

FIGURE 21. Projection on the horizontal (x, y)-plane of the three-dimensional trajectory of the buoy for time $t \in (0, 20\tau_I)$. The incident wave steepness is $k_I A = 0.13$; and the buoy is given a small initial displacement, $Y(0)/A = 10^{-6}$, from the vertical symmetry (x, z)-plane.

This research is financially supported by the Office of Naval Research (Ocean Engineering Division), under contract N00014-95-1-0010, monitored by Dr T. F. Swean Jr.

REFERENCES

DOMMERMUTH, D. G., LIN, W. M., YUE, D. K. P., RAPP, R. J., CHAN, E. S. & MELVILLE, W. K. 1988 Deep water plunging breakers: a comparison between potential theory and experiments. *J. Fluid Mech.* **189**, 423–442.

DOMMERMUTH, D. G. & YUE, D. K. P. 1987 A high-order spectral method for the study of nonlinear gravity waves. *J. Fluid Mech.* **184**, 267–288.

DOMMERMUTH, D. G. & YUE, D. K. P. 1988 The nonlinear three-dimensional waves generated by a moving surface disturbance. *Proc. 17th Symp. on Naval Hydro., Hague, Netherlands.* Washington DC: National Academy Press.

HOLMES, P. J. 1982 The dynamics of repeated impacts with a sinusoidally vibrating table. *J. Sound Vib.* **84**, 173–189.

LANDAU, L. D. & LIFSHITZ, E. M. 1959 *Theory of Elasticity*. Pergamon.

LIU, Y. 1994 Nonlinear wave interactions with submerged obstacles with or without current. PhD thesis, Massachusetts Institute of Technology.

LIU, Y., DOMMERMUTH, D. G. & YUE, D. K. P. 1992 A high-order spectral method for nonlinear wave–body interactions. *J. Fluid Mech.* **245**, 115–136.

LIU, Y. & YUE, D. K. P. 1998 On generalized Bragg scattering of surface waves by bottom ripples. *J. Fluid Mech.* **356**, 297–326.

MOON, F. C. 1992 *Chaotic and Fractal Dynamics: An Introduction for Applied Scientists and Engineers.* John Wiley & Sons.

NEWMAN, J. N. 1992 The Green function for potential flow in a rectangular channel. *J. Engng Maths* **26**, 51–59.

NEWMAN, J. N. 1993 Wave-drift damping of floating bodies. *J. Fluid Mech.* **249**, 241–259.

SCHWARTZ, L. W. 1974 Computer extension and analytic continuation of Stokes' expansion for gravity waves. *J. Fluid Mech.* **62**, 553–578.

Shaw, S. W. 1985 The dynamics of a harmonically excited system having rigid amplitude constrains. *Trans. ASME: J. Appl. Mech.* **52**, 453–464.

Tjavaras, A. A. 1996 The dynamics of highly extensible cables. PhD thesis, Massachusetts Institute of Technology.

Tjavaras, A. A., Zhu, Q., Liu, Y., Triantafyllou M. S. & Yue, D. K. P 1998 The mechanics of highly-extensible cables. *J. Sound Vib.* **213**, 709–737.

Triantafyllou, M. S. 1994 The dynamics of cables, chains and synthetic ropes for mooring applications. In *Behaviours of Off-shore Structures* (ed. C. Chryssostomidis). Cambridge, Massachusetts.

Triantafyllou, M. S. & Howell, C. T. 1994 Dynamic response of cables under negative tension: an ill-posed problem. *J. Sound Vib.* **173**, 433–447.

Tsai, W. T. & Yue, D. K. P. 1996 Computation of nonlinear free-surface flows. *Ann. Rev. Fluid Mech.* **28**, 249–278.

Wehausen, J. V. & Laitone, E. V. 1960 Surface waves. In *Handbuch der Physik*, vol. 9, pp. 446–478. Springer.

Wendroff, B. 1960 On centered difference equations for hyperbolic systems. *J. Soc. Indust. Appl. Maths* **8**(3), 549–555.

Wolf, A., Swift, J. B., Swinney, H. L. & Vastano, J. A. 1995 Determining Lyapunov exponents from a time series. *Physica* **116D**, 285–317.

Zakharov, V. E. 1968 Stability of periodic waves of finite amplitude on the surface of a deep fluid. *J. Appl. Mech. Tech. Phys.* **9**, 190–194 (English Transl.).